ANNUAL REPORT

to

OFFICE OF NAVAL RESEARCH

Contract USN 00014-94-I-0086

February 1995

PREDICTION OF HYDROGEN ENTRY AND PERMEATION IN METALS AND ALLOYS

H. W. Pickering
Department of Materials Science and Engineering
The Pennsylvania State University
University Park, PA 16802

PENNSTATE

College of Earth and Mineral Sciences

ANNUAL REPORT

to

OFFICE OF NAVAL RESEARCH

Contract USN 00014-94-I-0086

February 1995

PREDICTION OF HYDROGEN ENTRY AND PERMEATION IN METALS AND ALLOYS

H. W. Pickering
Department of Materials Science and Engineering
The Pennsylvania State University
University Park, PA 16802

REPORT DOCUMENTATION PAGE

Form Approved
OMB No. 0704-0188

1. AGENCY USE ONLY (Leave blank)	2. REPORT DATE	3. REPORT TYPE AND DATES COVERED
	February 1995	Annual 10/1/93 to 9/30/94

4. TITLE AND SUBTITLE

Prediction of Hydrogen Entry and Permeation in Metals and Alloys

5. FUNDING NUMBERS

N00014-94-I-0086

6. AUTHOR(S)

Howard W. Pickering

7. PERFORMING ORGANIZATION NAME(S) AND ADDRESS(ES)

The Pennsylvania State University
Department of Materials Science and Engineering
326 Steidle Building
University Park, PA 16802

8. PERFORMING ORGANIZATION REPORT NUMBER

9. SPONSORING/MONITORING AGENCY NAME(S) AND ADDRESS(ES)

Scientific Officer
Materials Division Code: 1131M
Office of Naval Research
Arlington, VA 22217-5000
ATTN: A. John Sedriks

10. SPONSORING/MONITORING AGENCY REPORT NUMBER

11. SUPPLEMENTARY NOTES

12a. DISTRIBUTION/AVAILABILITY STATEMENT

Approved for public release; distribution is unlimited.

12b. DISTRIBUTION CODE

13. ABSTRACT *(Maximum 200 words)*

This report summarizes results of the past year on our continuing experiments directed to the problem of hydrogen entry and degradation of materials both of planar surfaces and for the more complicated recessed surface. For the planar surface the hydrogen permeation and scanning tunneling microscopy (STM) techniques were used, and for the recessed surface the study used the hydrogen permeation technique and a microscopy/electrochemical probe technique. Microstructural effects and the role of microbes are also under study.

In aqueous solutions both IR drop and acidification within recesses in iron surfaces were found to enhance proton reduction and hydrogen absorption. In addition, it was found that flat, smooth surfaces can form or develop recesses as a result of corrosion or other reasons, e.g., grain boundary grooves that form during corrosion of Cr-depleted alloy in sensitized stainless steel. These recesses were found to be just as prone to proton discharge and hydrogen absorption as pre-existing recesses. Distributions of anodic and cathodic reaction sites were analyzed within a propagating crack under cathodic protection conditions using an IR based model. Results are presented of STM studies of hydrogen adsorption from the gas phase on silicon.

14. SUBJECT TERMS

KEY WORDS: hydrogen permeation cell, hydrogen absorption, IR drop and acidification effects, hydrogen evolution in recesses, corrosion-produced recesses, grain boundary grooves, scanning tunneling microscopy.

15. NUMBER OF PAGES

16. PRICE CODE

17. SECURITY CLASSIFICATION OF REPORT	18. SECURITY CLASSIFICATION OF THIS PAGE	19. SECURITY CLASSIFICATION OF ABSTRACT	20. LIMITATION OF ABSTRACT

TABLE OF CONTENTS

INTRODUCTION

This report is divided into four sections. Section 1 is a summary of progress and a list of project publications in the past year. Section 2 is a paper submitted to a leading electrochemistry/corrosion journal reporting on the generation of hydrogen in an anodically polarized sensitized ferritic stainless steel. The paper demonstrates that cavities, in this case grooves along the grain boundary that are created by anodic dissolution, can develop a critical aspect ratio that shifts the local electrode potential into the range for hydrogen evolution and hydrogen absorption into the steel. Section 3 is a paper presented at an international conference on hydrogen in materials which treats the effects of charge and mass transport limitations on the distributions of cathodic and anodic reactions on the flanks of environmentally induced cracks. Section 4 is a reprint of a paper published in a surface science journal describing the atomistics of hydrogen adsorption from the gas phase on clean silicon (100) surfaces.

SECTION 1

PROGRESS SUMMARY

The ongoing objective of this research project is to identify and evaluate the key factors which affect the process of hydrogen entry into metals (particularly steels) and their subsequent embrittlement under various service conditions, and to develop adequate remedial measures. This includes (i) identification of the conditions which lead to the generation of hydrogen within surface cavities that exist, for example, at the junctions of metals with other materials or at the surface intersections of inclusions in metals, or that form during service, e.g., crack propagation under open circuit or cathodic/anodic protection situations, (ii) the roles of metallurgical microstructure and solution species (H_2S) that promotes hydrogen adsorption in duplex stainless steels (AL 2205), and (iii) the influence of sulfate reducing bactering on the cathodic process and absorption of hydrogen in steel (in collaboration with D. D. Macdonald's ONR project).

An evaluation of the importance of the aspect ratio of cracks and other cavities has been one of the parameters under study during the past year. Aspect ratio is defined as the ratio of the depth

to opening dimension of a cavity. The aspect ratio can be independent of the actual depth of a cavity. Hence, a very shallow crack and a very deep crack may have the same aspect ratio. This result is readily obtained based on a modeling analysis in one of our earlier ONR sponsored research publications (Ateya and Pickering, 1975). Consequently, a shallow crack could, in principle, have the same IR drop as a deep crack since the magnitude of the IR is a function of the aspect ratio rather than simply of the crack depth. The consequences of this independence of aspect ratio and cavity depth has led to a working hypothesis on how stabilization of pit growth following passive film breakdown may occur (Xu et. al., in the list of Publications on the Project). The concept is equally powerful for the analysis of crack formation and stabilization during both cathodic and anodic polarization where either hydrogen absorption or metal dissolution may be responsible for the cracking event. A discussion of the aspect ratio in the context of potential distribution within localized corrosion processes is presented elsewhere (Pickering, J. Mat. Sci & Eng.).

Our focus on the generation of hydrogen gas within growing surface cavities (e.g., crevices and pits), and its subsequent absorption and embrittlement of the metal involves considerable amounts of mathematical modeling and experimental testing. Available results have been published in several key papers during the last few years (Kelly, et al., Nystrom, et. al., Xu, et. al., Ateya, et. al.), two of which constitute Sections 2 and 3 of this report and the others are in the Jan. 93 Annual Report and Final Report for 10/1/90 to 9/30/93. Some of the consequences of these studies for metallic surfaces under cathodic polarization impact on the need for an improved analytical characterization method for predicting (i) the success or failure of cathodic protection of recesses, (ii) the occurrence of active dissolution at the crack tip and adjacent crack flanks, and (iii) the distribution of hydrogen charging rate on the crack flanks.

PUBLICATIONS ON THE PROJECT

W. Kelly, R. N. Iyer and H. W. Pickering, "Another Grain Boundary Corrosion Mechanism in Sensitized Stainless Steel", J. Electrochem. Soc., 140, 3134-3140 (1993).

Yuan Xu, Minghua Wang and H. W. Pickering, "On Electric Field Induced Breakdown of Passive Films and IR Voltage Stabilization of Pitting Corrosion", J. Electrochem. Soc., 140, 3448-3457 (1993).

K. Cho and H. W. Pickering, "The IR Drop Mechanism of Crevice Corrosion", pp. 1277-1282 in The Proceedings of the International Conference for Korean Scientists and Engineers, Volume of Materials and Chemistry, ed., S. J. Kim, KOFST, Korea (1993).

E. A. Nystrom, J. B. Lee, A. A. Sagüés and H. W. Pickering, "An Approach for Estimating Anodic Current Distributions in Crevice Corrosion from Potential Measurements", J. Electrochem. Soc., 141, 358 (1994).

E. A. Nystrom, A. A. Sagüés and H. W. Pickering, "Current and Potential Distributions Inside Crevices in Rebar Steel and Other Metals", in the Proceedings of the 1st Mexican Symposium and 2nd International Workshop on Metallic Corrosion, Mérida, Yucatán, México, March 1994.

H. W. Pickering, "The Role of Electrode Potential Distribution in Corrosion Processes", J. Materials Sci. & Eng. A, in print.

B. G. Ateya and H. W. Pickering, "Distribution of Anodic and Cathodic Reaction Sites During Environmentally Assisted Cracking", Hydrogen Effects on Material Behavior, A. W. Thompson and N. R. Moody, eds., The Minerals, Metals and Materials Soc., Warrendale, PA 15086.

M. Wang, H. W. Pickering and Y. Xu, "Potential Distribution, Shape Evolution and Modeling of Pit Growth for Ni in Sulfuric Acid", submitted to J. Electrochem. Soc.

A. Sehgal, B. G. Ateya, R. N. Iyer and H. W. Pickering, "Hydrogen Generation in an Anodically Polarized Sensitized Ferritic Stainless Steel", submitted to J. Electrochem. Soc.

A. Sehgal, B. G. Ateya and H. W. Pickering, "Hydrogen Charging from Within Grain Boundary Grooves", A. Sehgal, B. G. Ateya and H. W. Pickering, to be submitted to the J. Electrochem. Soc.

SECTION 2

HYDROGEN GENERATION IN AN ANODICALLY POLARIZED SENSITIZED FERRITIC STAINLESS STEEL

A. Sehgal, B. G. Ateya, R. N. Iyer and H. W. Pickering

Department of Materials Science and Engineering
The Pennsylvania State University
University Park, PA 16802

Abstract

This paper presents evidence for the electrolytic generation of hydrogen within the grain boundary grooves inside membranes of sensitized 430 stainless steel while the sample's outer surfaces are anodically polarized with respect to the equilibrium potential of the hydrogen evolution reaction (HER). The grooves are formed by the dissolution of the chromium depleted zone adjacent to the precipitated chromium carbides. This indicates that the local electrode potential within the grain boundary grooves is considerably less noble than that applied at the outer surface and indeed lower than that of the HER. An IR potential shift mechanism explains the results. It is shown that this IR phenomenon creates the conditions for hydrogen embrittlement within the steel for the existing electrochemical conditions at the outer surface which prohibit hydrogen generation.

INTRODUCTION

Recent work on sensitized 430 stainless steel (430 SS) has proved the existence of a second corrosion process occurring during intergranular corrosion under conditions of anodic polarization of the steel surface.[1,2] The process is characterized by greater subsurface dissolution than expected, specifically anodic dissolution of the bulk alloy occurred rather than only of the Cr-depleted alloy, and by gas evolution from within the resulting grain boundary grooves. These results were attributed to a localized corrosion process set up by the IR drop within the electrolyte of the grain boundary groove.[2] In this explanation the IR drop shifts the local electrode potential within the grooves into the active dissolution region of the bulk alloy.[3,4] The observed gas evolution from within the grain boundary grooves is also indicative of a local electrode potential that is considerably less noble than that applied at the outer surface of the specimen if the gas is hydrogen.[2] The evolving gas was deduced to be hydrogen based on similar experiments on pitting[3] and crevice corrosion of iron.[4] In the pitting investigation,[3] the gas emanating from the pits was collected and found to be hydrogen by analysis in a mass spectrometer.

The purpose of this work is to establish that the electrolytically produced gas within the grain boundary grooves is hydrogen by detecting hydrogen in the metal. This was done by testing sensitized 430 SS membranes in the Devanathan-Starchurski cell[5] to detect the hydrogen generated within the steel membranes while both of its surfaces were maintained at anodic potentials which prohibit the HER.

EXPERIMENTAL

Membranes of type 430 SS (wt % Cr - 1 6.46, C - 0.055, Mn - 0.48, Mo - 0.024, N - 0.017, Ni - 0.32, P - 0.035, S - 0.004, Si - 0.36, Fe - balance) were cold rolled to 0.037 mm thickness and solution annealed at 1200°C for 1 hour and ice water quenched. Sensitization was induced by heating at 550°C for two hours followed by an ice water quench.

A Devanathan-Starchurski cell[5] was used to detect any electrolytically produced hydrogen that may have entered the metal from within the grain boundary groove. An area of 0.8 cm^2 of each surface of the membrane was exposed to the electrolyte. The "charging" side of the membrane (in cell 1) was anodically potentiostated at a potential of 192 mV (NHE) in deaerated 1 N H_2SO_4 (pH = 0.36). A saturated calomel electrode was used as the reference electrode in cell 1 along with an agar salt bridge to prevent the ingress of chloride ions from the calomel electrode into the electrolyte.

The "exit" surface of the membrane (in cell 2) was coated with Pd to prevent oxidation of the underlying membrane. An acid solution (1 N H_2SO_4 + 3 x 10^{-4} M $K_3Fe(CN)_6$, pH = 0.36) was used in cell 2 instead of the normally used basic solution. The potassium ferricyanide was added to the "exit" solution to detect iron. If the grain boundary grooves produced on the "charging" surface (cell 1) continued to grow, eventually penetrating the sample thickness and thus, arriving at the passively maintained "exit" surface, then the iron dissolving in the groove would be detected as prussian blue spots formed by the reaction between ferrous and ferricyanide ions.[6] The "exit" surface was continuously monitored for prussian blue spots using a mirror placed in cell 2 and a high intensity light source. The presence of potassium ferricyanide was not found to affect the polarization curve for the sensitized steel. A Hg/Hg_2SO_4 electrode was used to maintain the potential at 642 mV(NHE) for the solution in cell 2. This electrode potential was chosen so that even if the Pd layer did not fully protect the steel, both the Cr-depleted and bulk alloy would be passivated while ensuring complete oxidation of any hydrogen atoms arriving at the "exit" surface. Use of potentials ± 100 mV of 642 mV (NHE) gave identical results during background current decay. Hence, it was concluded that all the hydrogen atoms arriving at the "exit" surface was

oxidized at this potential. Two Wenking 75 LB M potentiostats were used to maintain the potentials on either side of the membrane. Purified argon gas was used to deaerate the cell compartments. Further details about the cell, equipment and procedures are reported elsewhere.[7,8]

RESULTS AND DISCUSSION

Figure 1 shows the measured anodic polarization curve of the sensitized stainless steel in 1 N H_2SO_4. The figure shows a secondary anodic maximum at 142 mV (NHE). This has been attributed to the superposition of two anodic currents, one from the bulk alloy and the other (the major current density) from a chromium-depleted zone adjacent to the grain boundary.[2,8-11] The second maxima extends from 10 to 300 mV NHE.[8] The surface of the sensitized steel in cell 1 was maintained at 192 mV (NHE) to form the grain boundary (g.b.) grooves by dissolution of the Cr-depleted zones which lie along the grain boundaries. This potential is about 200 mV more noble than the equilibrium potential of the HER in the 1N H_2SO_4 solution. Details of the metallographic characterization of these grooves are reported elsewhere.[8]

Figure 2 shows the hydrogen permeation transient observed for a 0.032 cm thick sensitized 430 SS anodically polarized at 192 mV (NHE). Three different stages can be identified in the transient. In the first stage, that lasted about 900 minutes, no permeation current could be detected. In the second stage, that lasted ~ 250 minutes, a very small permeation current was detected. In the final stage the permeation current showed an exponential increase. During the first and second stages no prussian blue spots were observed on the "exit" surface. A blue spot became visible during the final stage of the transient at 1170 minutes.

Figure 3 shows a cross-sectional micrograph of a membrane polarized at 192 mV (NHE) in cell 1. The experiment was stopped after a permeation current of 0.05 μA was recorded in cell 2. It is clear that the grain boundary grooves that form on the surface in cell 1 penetrate only part of the thickness of the membrane. This micrograph is typical of all of the samples except that the depth of penetration of the g.b. grooves varied from sample to sample, being deeper the longer the time of the test.

The permeation transient shown in Figure 2 is much different from that normally recorded under conditions of cathodic hydrogen charging of the external surface of a membrane,[5,7] where one obtains an s-shaped curve with a diffusion limited plateau. The progressively increasing rate

of hydrogen permeation points to the generation of hydrogen over more and more area of the g.b. grooves as the grooves increase in depth within the membrane.

The time lag observed in region 1 is the sum of two components associated with the various processes forming the operating mechanism, i.e.,

(i) The time required to dissolve the Cr-depleted zone and to generate grain boundary grooves of sufficient depth and aspect ratio[12] to set up a large enough ohmic potential drop within the grooves so that hydrogen ion reduction, hydrogen absorption and the HER could take place.

(ii) The time taken for the hydrogen absorbed in the metal lattice to diffuse from the location where it was absorbed (within the g.b. groove, cell 1) to the Pd coated "exit" surface of the membrane where it is oxidized (cell 2).

The above components of the "time lag" cannot be separated easily, even though each of them is associated with a distinct process.

CONCLUSIONS

1. Detection of a hydrogen permeation current (cell 2) from a sample whose outer surface (cell 1) was potentiostated at an anodic potential (oxidizing with respect to hydrogen) proves that the local electrode potential inside the anodically produced grain boundary grooves had shifted more than 200 mV in the less noble direction into the potential regime of the HER. Thus, hydrogen ion reduction and its absorption into the metal produced the permeation current while at the outer surfaces (cells 1 and 2) the HER was prohibited. The evolution of gas bubbles from within the grooves shows that some of the other adsorbed hydrogen atoms combined to form hydrogen gas inside the grooves.
2. The grooves form by the dissolution of the chromium depleted zone adjacent to the precipitated chromium carbides in the sensitized stainless steel. For a depth-to-opening dimension (aspect ratio) of the g.b. groove that produced a sufficiently large IR, the HER and hydrogen absorption occurred at that depth, and then the absorbed hydrogen diffused to the outer surfaces including the "exit" surface (cell 2) where its arrival was detected by the oxidation current in cell 2. The formation of the grooves contributed to the total time lag for arrival of hydrogen at the "exit" surface.

ACKNOWLEDGMENT

The authors gratefully acknowledge the financial support of the Office of Naval Research, under Grant No: N00014-94-1-0086 (A. J. Sedriks).

REFERENCES

1. B. W. Bennett and H. W. Pickering, Met. Trans. A, 18A, 1117 (1987).
2. W. Kelly, R. N. Iyer and H. W. Pickering, J. Electrochem. Soc., 140, 3134 (1993).
3. H. W. Pickering and R. P. Frankenthal, J. Electrochem. Soc., 119, 1297 (1972).
4. K. Cho and H. W. Pickering, J. Electrochem. Soc., 137 , 3313 (1990); ibid, 138, L56 (1991).
5. M. A. V. Devanathan and L. Starchurski, J. Electrochem. Soc., 111, 61 (1964).
6. D. A. Skoog and D. M. West, Analytical Chemistry, 3rd ed., Saunders College Publisher, Philadelphia, PA, p. 466 (1980); P. Hersch, J. B. Hare, A. Robertson and S. M Sutherland, J. Appl. Chem., 11, 246 (1961).
7. S. S. Chatterjee, B. G. Ateya and H. W. Pickering, Met. Trans., 9A, 389 (1978).
8. A. Sehgal, Ph.D. Thesis, The Pennsylvania State University, 1995.
9. M. B. Rockel, Corrosion, 27, 95 (1971).
10. P. Suery and T. Geiger, Werkstoffe und Korrosion, 20, 665 (1969).
11. J. A. Dobbelaar, E. C. M. Herman and J. H. de Wit, Corr. Sci., 33, 779 (1992).
12. Y. Xu, M. Wang and H. W. Pickering, J. Electrochem. Soc., 140, 3448 (1993).

FIGURE CAPTIONS

Figure 1. Measured anodic polarization curve for sensitized Type 430 stainless steel in 1N H_2SO_4, and a schematic of the HER curve..

Figure 2. Measured hydrogen permeation current at the Pd coated "exit" surface for a membrane with both of its surfaces anodically polarized with respect to the HER. E_{cell1} = 192 mV and E_{cell2} = 642 mV (NHE).

Figure 3. Cross section optical micrograph showing an example of groove formation that established a sufficiently large IR drop for the occurrence of the HER inside the groove.

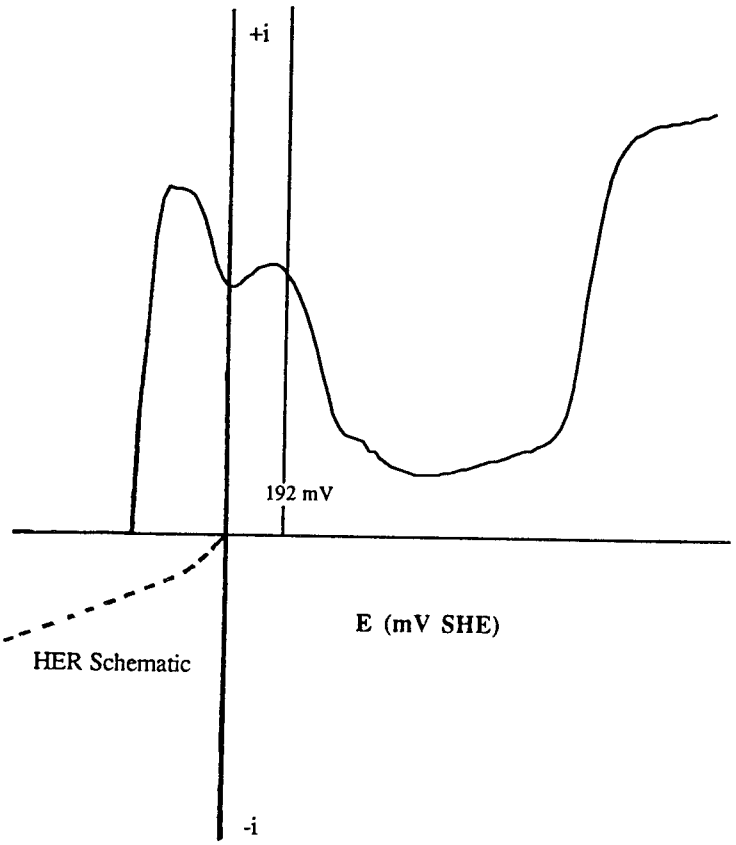

Figure 1

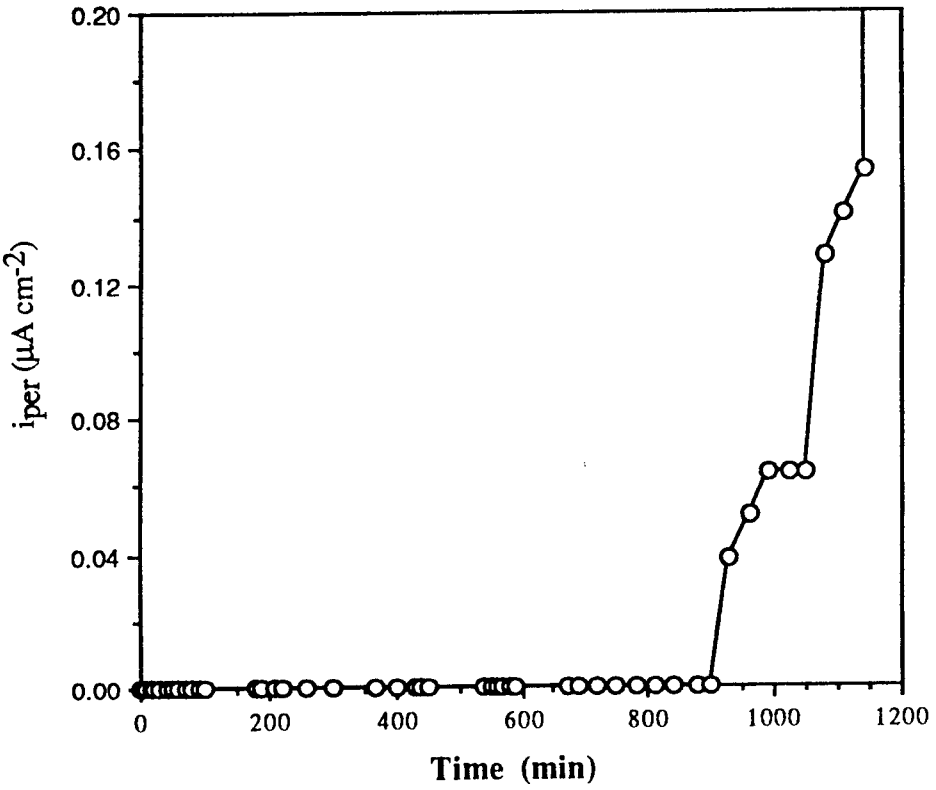
0.20
0.16
0.12
0.08
0.04
0.00
i_{per} (μA cm^{-2})
0
200
400
600
800
1000
1200
Time (min)

Figure 2

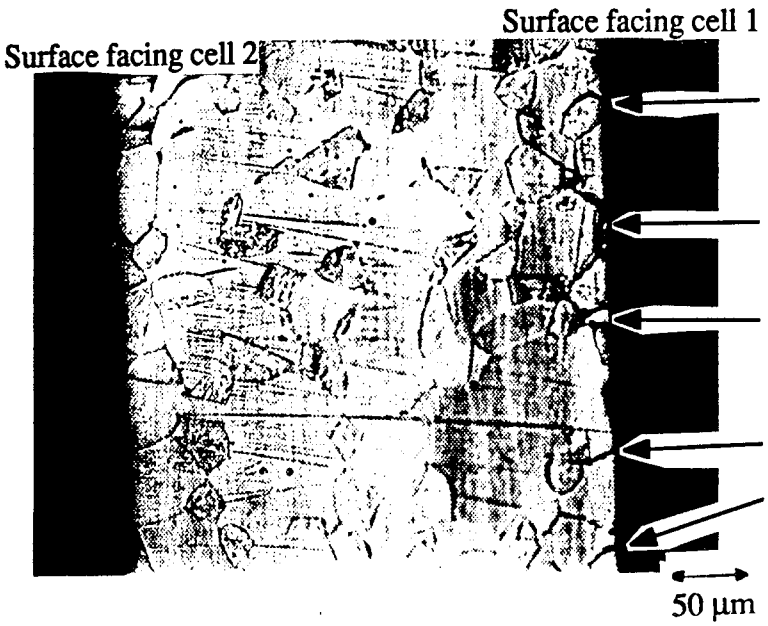

Figure 3

Hydrogen Effects on Material Behavior,
A. W. Thompson and N. R. Moody, ed., TMS, Warrendale, PA (1995)

DISTRIBUTIONS OF ANODIC AND CATHODIC REACTION SITES

DURING ENVIRONMENTALLY ASSISTED CRACKING

B. G. Ateya[1] and H. W. Pickering

Department of Materials Science and Engineering
The Pennsylvania State University
University Park, PA 16802

Abstract

This paper treats the effects of charge and mass transport limitations on the distributions of cathodic and anodic reactions on the flanks of environmentally assisted cracks. Under conditions of cathodic protection of the metal surface, it is shown that the presence of recesses or cracks leads to significant changes in the potential and ionic concentrations at various distances into the cavity. Consequently, the rate of the hydrogen evolution reaction decreases with increasing distance into the cavity. Furthermore, for active metals e.g., Fe or Ni, metal dissolution occurs with progressively increasing rates at increasing distance into the crack. The variations of these cathodic and anodic current distributions with distance within the crack (or with the time of cracking) depends on the dimension of the opening of the crack *a*, the diffusivity of the hydrogen ion, D_{H^+}, and, hence, the conductivity of the electrolyte, and the polarization at the external surface of the metal, $\eta(0)$. Analysis of the migration-diffusion problem leads to the development of a characteristic depth given by

$$Z = \left[\frac{F D_{H^+} c^{o}_{H^+} a}{i_{oH}} \exp\frac{(\beta\eta(0))}{b}\right]^{1/2} \text{cm}$$

where $c^{o}_{H^+}$ is the acid concentration, and β and i_o are the charge transfer coefficient and the exchange current density of the hydrogen evolution reaction, respectively. Z has a strong effect on the behavior of the system.

---

[1] Permanent address: Chemistry Department, Faculty of Science, Cairo University, Egypt.

Introduction

The mechanism of environmentally induced cracking of metals and alloys is attracting ever-increasing attention. Several conference proceedings and review articles have been published (1-3) which review the literature and project the present state of understanding of this issue. The phenomenon necessarily involves complex interactions between the prevailing environment and the electrode potential at the alloy surface with its microstructural features under the effects of stress. It is now widely recognized that the chemical and electrochemical conditions within cavities or cracks (and actually at the tip of such cracks) in metals and alloys are different from those at the external surface (4-6). Over the years, this recognition led to the evolution of a general belief that the anodic and the cathodic reactions are spatially separated, i.e., when the anodic reaction occurs within a pit, crevice or a crack, the cathodic reaction occurs at the outer surface and vice versa. This assumption has been frequently used in modeling the cracking and pitting processes (7-9). It will be shown below that well-separated anodic and cathodic reactions is only a limiting case which is encountered in early stages of crack growth. The general case for base metals involves distributions of both the anodic and cathodic (hydrogen evolution) reactions, with various intensities at different locations on the internal surfaces of the cracks, along with the reduction of an oxidant at the outer surface for the special case of a freely corroding metal. This more complicated situation is a result of the combined effects of the potential distribution (IR) down the crack and the polarization characteristics of the particular system. It is also shown that at a later stage of cracking in active (base) metals, the situation might well reach the other limit, i.e., where both the anodic and cathodic (hydrogen evolution) reactions occur simultaneously at the same place and at the same rate deep within the crack, under a mixed potential established by the particular metal/hydrogen evolution system existing inside the crack.

The objective of this paper is to present and explore the relations which govern the distributions of anodic and cathodic reactions on the internal surfaces of cracks that propagate inward from the sample surface, and the dependence of these distributions on crack geometry, the electrochemical parameters of the system, the properties of the prevailing environment and the electrode potential at the alloy surface. These distributions are shown to vary with the time of propagation of, and the distance within, the crack.

Potential Drop within Cracks: Causes and Consequences

When a cracked metal surface is held under a certain electrode potential, E(0), the flanks of the crack are usually under different "local" values of electrode potential, E(x), where x is the distance into the crack. Figure 1 illustrates this situation, for a rectangular crack (10). The magnitude of the potential difference is given by

$$\Delta E(x) = E(0) - E(x) = \varphi(x) \tag{1}$$

where $\phi(x)$ is the local galvani potential difference in the electrolyte which fills the crack, i.e., $\phi(x) = 0$ at $x = 0$. The magnitude and sign of $\Delta E(x)$ depend on the distance down the crack x, the crack opening a, the magnitude and sign of the current density at the outer surface (i_s) supported by the potential at the outer surface, E(0), and the resistivity of the electrolyte path from $x = 0$ to x. This potential difference occurs in the electrolyte phase. It drives the ionic current through the resistivity of the electrolyte path within the crack. This ionic current is equivalent to the sum of the faradaic currents which result from the electrochemical charge transfer reactions occurring on the flanks of the crack. The magnitude of this potential difference is given by

$$\varphi(x) = \int_0^x I(x)\rho(x)dx \tag{2}$$

where I(x) is the local ionic current density flowing in the x direction through the electrolyte that fills the crack, and $\rho(x)$ is the local resistivity of the electrolyte path at x. The relation between E(x) and E(0) is given by:

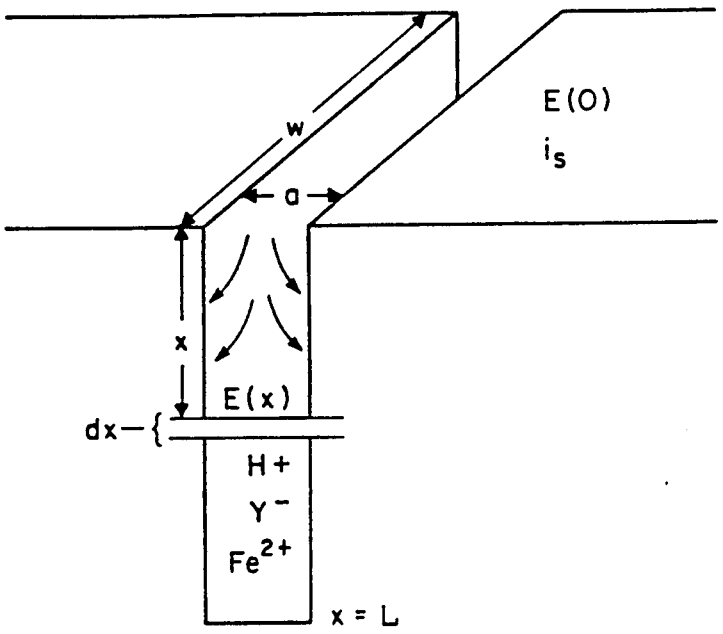

Figure 1. Model of a crack in which the HER occurs on the outer surface (i_s) and on the crack walls. The bulk electrolyte is H^+ and Y^- and the outer (x = 0) surface conditions are E (0) and i_s.

$$E(x) = E(0) - \int_o^x I(x)\rho(x)dx \qquad (3)$$

Equation 3 is written such that the ionic current density I has a positive sign for anodic currents and a negative sign for cathodic currents. The consequences of Equation 3 can be far-reaching, depending on the magnitude of the IR term. For instance under the local potential value of E(x), one or the other of the following possibilities occur:

i. The current density i(x) on the flanks of the crack, representing the rate of the half cell reaction occuring at x, becomes significantly different (up to an order of magnitude) from that at the external surface, i_s, under E(0). The local current density i(x) may be greater or smaller than i_s at the outer surface, depending on the particulars of the system.

ii. For cracks in active metals, e.g., Fe or Ni, another electrochemical reaction takes place if favored by its polarization behavior and the local value of E(x). In that respect, if the crack tip is under a potential E(x), it might well encounter electrochemical reaction(s) different in nature and rate than those occurring at the outer surface of the metal.

We present below some of the governing equations and use them to illustrate the distributions of anodic and cathodic reaction rates at different distances within cracks under cathodic polarization conditions. The effects of crack geometry (aspect ratio, $L\,a^{-1}$ in Fig. 1), extent of polarization, and the transport properties of the electrolyte on these distributions, will be illustrated and discussed.

The Test System

The discussion is presented below for a system of iron in sulfuric acid, for which the computed polarization curve is shown in Figure 2a. This figure was constructed using the following rate equations for both the metal dissolution and the hydrogen evolution (HER) reactions:

(a)

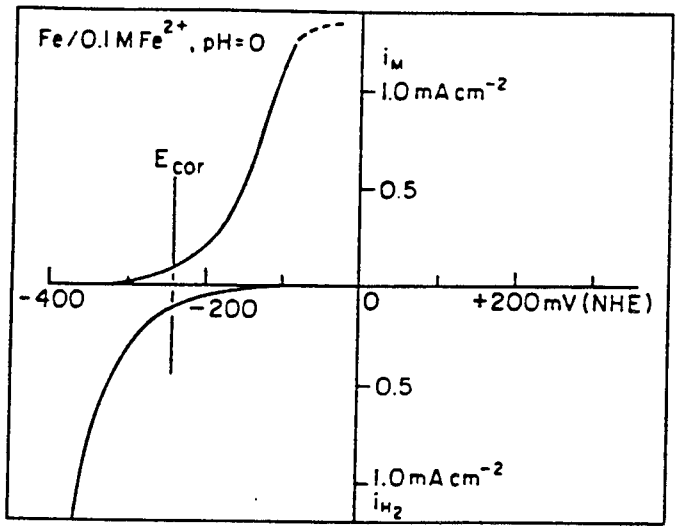

(b)

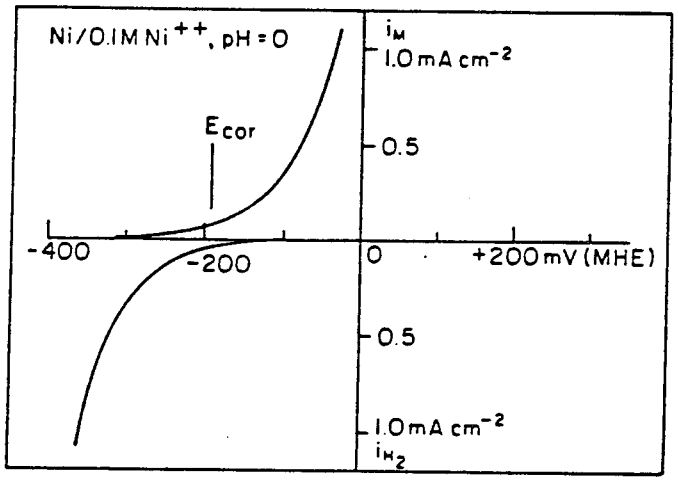

(c)

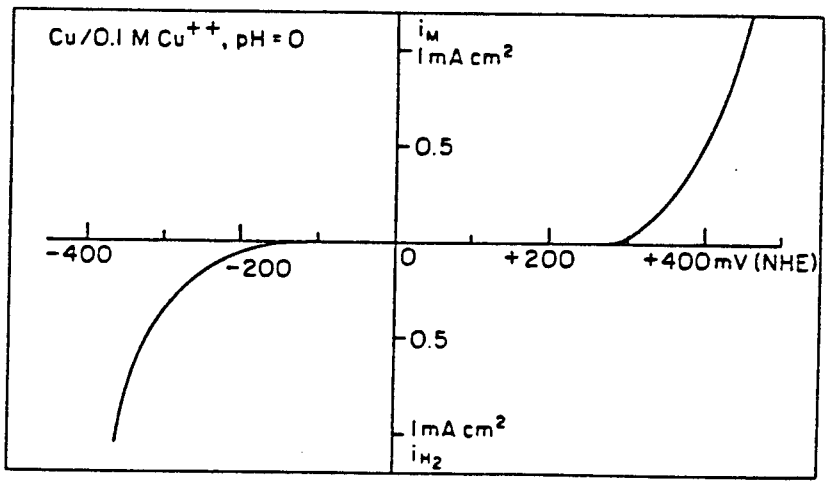

Figure 2. Illustration of the partial anodic and cathodic currents for the system: (a) Fe/0.1M Fe^{2+} in 1N acid, (b) Ni/0.1M Ni^{++} in 1N acid, (c) Cu/0.1M Cu^{++} in 1N acid.

For $$Fe_{(s)} \rightarrow Fe^{2+}_{(aq)} + 2e^- \quad (4)$$

$$i_{Fe} = i_{oFe}\,[\exp(\alpha n\eta(Fe)/b) - \exp(-(1-\alpha)n\eta(Fe)/b)] \quad (5)$$

where i_{Fe} is the metal dissolution current per unit of metal surface area, $\eta(Fe)$ is the polarization driving the metal dissolution reaction, $b = RT/F$ and α, n and i_{Fe} are the charge transfer coefficient, the number of electrons and the exchange current density of this reaction, respectively. For the hydrogen evolution reaction (HER) i.e.,

$$2H^+ + 2e^- \rightarrow H_2\,(g) \quad (6)$$

the rate is given by

$$i_H = i_{oH}\,[\exp(-\beta\eta(H)/b) - \exp(-(1-\beta)\eta(H)/b)] \quad (7)$$

where i_H, i_{oH}, β, and $\eta(H)$ refer to the current density, exchange current density, charge transfer coefficient and the overpotential (polarization), driving the HER. The polarization curves in Figure 2 were computed using typical values, i.e., $i_{oFe} = i_{oH} = 10^{-6}$ A cm^{-2}, $b = \alpha n = 0.5$ and E_{rev} (Fe/Fe^{2+}) = -0.470 V(NHE) which corresponds to 0.1 M Fe^{2+} ions. The E_{rev} (H_2/H^+) was taken to be 0.0V (NHE), i.e., pH = 0. With this form of Equations 5 and 7, the cathodic polarization has a negative sign while the anodic has a positive sign. Note that there is a fairly broad region of potential over which reactions 4 and 6 occur simultaneously albeit at different rates. In principle, this range extends from $E_{rev}(Fe/Fe^{2+})$ to $E_{rev}(H_2/H^+)$, i.e., from -470 mV (NHE) to 0 mV (NHE). The free corrosion potential of this system is the potential at which both the anodic metal dissolution and cathodic hydrogen evalution currents are equal (11).

The corresponding situations for Ni and Cu are shown in Figs. 2b and c. For Ni the potential range, over which both nickel dissolution and hydrogen evolution occur simultaneously, (from -280 to 0 mV), is much less than in the case of Fe. The case of Cu represents a limit in that both the anodic copper dissolution and cathodic hydrogen evalution reactions cannot occur simultaneously. In fact, they are separated by about 350 mV on the potential coordinate. These figures will prove to be most useful in a discussion of the significance and consequences of potential shifts within cracks.

Transport Equations

We will consider a model system of a rectangular crack in an iron surface exposed to a dilute acid solution. Allowance is made for one-dimensional mass transport by diffusion and ionic migration in the x-direction into the crack. We also use the transport relations of dilute electrolytes. No allowance will be made here for the additional effects of hydrolysis (localized acidification) or complexation of metal ions, gas bubbles, formation of salt film, etc. However, we do allow for an important factor which has been frequently ignored, i.e., the distribution of the electrochemical reactions on the walls of the crack. We also formulate the equations assuming a pseudo-steady state. This assumption is justified in view of the following order of magnitude calculation. Let us consider that the crack propagates 1 cm in 10^7 s. Then, taking an average diffusivity of ions within the electrolyte of $D \simeq 10^{-5}$ cm^{2}s^{-1}, the root mean square displacement during this time is $\sqrt{\overline{x^2}} \simeq \sqrt{2\times10^{-5}\times10^7} \simeq 14$ cm. Thus, the rate of mass transfer (14×10^{-7} cm s^{-1}) is much faster than that of crack propagation for values of the crack propagation speed lower than 10^{-7} cm s^{-1}.

Performing a mass balance, on the various ionic species, on a space element dx, as shown in Figure 1, one obtains

$$j_{H^\cdot} = -D_{H^\cdot}\left[\frac{dc_{H^\cdot}}{dx} + c_{H^\cdot}\frac{F}{RT}\frac{d\phi}{dx}\right] = \frac{I_{H^\cdot}}{F} \quad (9)$$

$$j_{y^-} = -D_{y^-}\left[\frac{dc_{y^-}}{dx} - c_{y^-}\frac{F}{RT}\frac{d\varphi}{dx}\right] = 0 \tag{10}$$

$$j_{Fe^{2+}} = -D_{Fe^{2+}}\left[\frac{dc_{Fe^{2+}}}{dx} + 2c_{Fe^{2+}}\frac{F}{RT}\frac{d\varphi}{dx}\right] = -\frac{I_{Fe^{2+}}}{2F} \tag{11}$$

where the j's refer to the ionic fluxes through the electrolyte in the crack as a function of distance x, c and D refer to the concentration and diffusivity, respectively, of the various ionic species and φ is the potential drop into the crack (Equation 1). With this formulation of the problem, it follows that $\varphi > 0$ for anodic polarizations and $\varphi < 0$ for cathodic polarizations. All the variables in Equations 9 to 11, (i.e., the c's, I's and φ) are functions of distance, x. The concentration terms are also subject to the electroneutrality condition, i.e.,

$$c_{H^+} + 2c_{Fe^{2+}} = c_{y^-} \tag{12}$$

These fluxes are supported by the electron transfer reactions taking place on the flanks of the crack. The rates of these reactions are related to the local value of electrode potential and the electrode kinetics of the particular reaction by the Butler-Volmer equation. Considering the space element, dx, in Figure 1, one obtains

$$dI_{H^+} = \left(\frac{2}{a}\right) i_H(x)dx$$

$$= \left(\frac{2}{a}\right) i_{oH}\left[\exp(-\beta\eta(H)/b) - \exp(-(1-\beta)\eta(H)/b)\right] dx \tag{13}$$

and

$$dI_{Fe2+} = \left(\frac{2}{a}\right) i_{oFe}\left[\exp(\alpha n\eta(Fe)/b) - \exp(-(1-\alpha)n\eta(Fe)/b)\right] dx \tag{14}$$

where I_{H^+}, β and $\eta(H)$ are, respectively, the ionic current density resulting from the flow of H^+ ions within the electrolyte that fills the crack in the x direction (Fig. 1), the charge transfer coefficient of the HER and the polarization driving the HER. Similarly, I_{Fe2+}, α and $\eta(Fe)$ are the corresponding parameters for the metal dissolution reaction. The polarizations, $\eta(H)$ and $\eta(Fe)$, are given by

$$\eta(H) = E(0) - \varphi(x) + 0.059\ pH \tag{15}$$

$$\eta(Fe) = E(0) - \varphi(x) - E_{rev}(Fe/Fe^{2+}) \tag{16}$$

where the $E_{rev}(Fe/Fe^{2+})$ is the reversible potential of iron in the particular medium.

The boundary conditions of the system are defined in terms of ionic concentrations and current or potential at the external surface. Thus, at $x = 0$,

$$c_{Fe2+} = 0,\ c_{y^-} = c_{H^+} = c^o \tag{17}$$

and at E(0),

$$i_H \text{ and } i_{Fe} = f(\text{polarization curves}) \tag{18}$$

We now have six equations (9 to 14) and six variables (c_{H^+}, c_{y^-}, c_{Fe2+}, I_{H^+}, I_{Fe2+} and ϕ).

The literature has no reference to a complete solution to this system of equations. Solutions for various limiting cases have been reported. Several such solutions assumed passive or inert flanks of the cracks, and hence they ignored the distribution of the electrochemical reactions on these flanks (7-9). We present below some of the solutions which allow for these distributions, albeit

for some limiting cases. In order to bring out the physical significance of, and the inter-relationships among, the various parameters and variables of the system, we will discuss the cases where analytical solutions to the equations were obtained.

Cathodic Polarization

Under conditions of cathodic polarization of the external metal surface at a potential E(0) which supports a cathodic current (i_s) at the outer surface, and assuming that only the HER is taking place within the crack, the system is governed only by Eqs. 9 and 10. An analytical solution to this system is available in the literature (10). The potential, ionic concentration and current distributions are given by (10):

$$\phi(x) = \frac{RT}{F} \ln \frac{\cosh[(L-x)/Z]}{\cosh[L/Z]} \tag{19}$$

$$c(x) = c^{\circ} \frac{\cosh[(L-x)/Z]}{\cosh[L/Z]} \tag{20}$$

$$i(x) = i_s \frac{\cosh[(L-x)/Z]}{\cosh[L/Z]} \tag{21}$$

where L is the crack depth and Z (in cm) is a characteristic depth given by

$$Z = [F D_{H^+} c^{o}_{H^+} a / i_s]^{1/2} \tag{22}$$

Note that the characteristic depth Z includes the system parameters relating to: (i) the electrode kinetics and potential driving the HER (via i_s and Equation 7), (ii) the width of the crack opening a, which determines the aspect ratio $L\,a^{-1}$, (iii) the concentration and the diffusivity of hydrogen ions in, and conductivity of, the electrolyte (via the product $D_{H+}\,c^{o}_{H+}F$). It will be shown below that the characteristic depth Z determines the behavior of the system. Note also that the current i_s - is related to the potential E(0) at the external surface of the metal through Equation 7. Upon substituting for i_s from Equation 7 (assuming the polarization is sufficiently large to ignore the reverse reaction), one obtains

$$Z = \left[\frac{F D_{H+}\, c^{o}_{H^+} a}{i_{oH}} \exp \frac{(\beta \eta(0))}{b}\right]^{1/2} \text{cm} \tag{23}$$

Thus, a decrease in the magnitude of the crack opening dimension a and/or an increase in the magnitude of cathodic polarization $\eta(0)$ which drives the reaction at the external surface (and which has a negative sign) lead to a decrease of the value of Z. A similar characteristic depth Z has frequently been used in studying the current distributions during the electroplating within cracks or scratches (12).

For the sake of a quantitative calculation, let us consider the case of an iron surface cathodically protected under a potential of - 0.5V (NHE) in an electrolyte solution of pH = 3 at 25°C. This value is comparable to the -0.8V ($Cu/CuSO_4$) which is commonly used in the practice of the cathodic protection of steel. Assuming the transfer coefficient is $\beta = 0.5$ and the exchange current density, i_o, of the HER is 10^{-8} A cm^{-2}, it follows that the value of $i_s \approx 5.5 \times 10^{-6}$ A cm^{-2}. Using values of $D_{H^+} = 10^{-5}$ cm^2 s^{-1}, $c^{\circ} = 10^{-6}$ mole cm^{-3}, F = 96487 C eq^{-1} and $a = 10^{-2}$ cm, Z = 0.042. We have calculated the current and potential distributions under various conditions for several combinations of L (from 10^{-3} to 1 cm) and Z (from 0.004 to 0.04 cm). The results are presented below.

Figure 3 illustrates the potential and (cathodic) current distributions within cracks of different depths ranging from L=10 μm to 1 cm, for a value of characteristic depth, Z = 0.04 cm. The distance coordinate uses a logarithmic scale to accommodate the broad range of values of crack length. Furthermore, it gives a measure of the cracking time. Assuming a constant value of the crack propagation speed, e.g., 10^{-7} cm s^{-1}, one can easily calculate the cracking time. To that extent, the calculations give the time variations of the spatial potential and current distributions on the flanks of the crack. The pH within the crack also changes, becoming more alkaline with distance into the crack as given by Eq. 20. If the aspect ratio is favorable for formation of Fe^{2+} ions, the pH will rise to a limiting value which is the equilibrium pH of the hydrolysis reaction as discussed elsewhere (13).

Figure 3 reveals that as the distance within the crack (or the cracking time) increases, the local cathodic (HER) current density decreases while the magnitude of the galvani potential difference in the electrolyte, $\phi(x)$, increases. Since $\phi(x)$ is negative, Eq. (1) requires that the local electrode potential E(x), shifts in the (less negative) more noble direction with increasing distance into the crack. Two potential scales are used on the right coordinate of Figure 3; one for the IR drop in the crack electrolyte, $\phi(x)$, and the other for the local electrode potential, E(x). As the distance within the crack increases (for constant Z), the magnitude of $\phi(x)$ increases (while $\phi(x)$ is negative in value), i.e., we have a greater shift of the local potential E(x) in the more noble (less negative) direction. No iron dissolves as long as E(x) is negative of E_{rev} (Fe/Fe^{2+}), which is -0.470V (NHE) for the present case while hydrogen is evolved profusely under this potential. As E(x) becomes equal to or positive of E_{rev} (Fe/Fe^{2+}), iron dissolution occurs along with hydrogen evolution, at rates dependent on the position of E(x) on the potential coordinate in Figure 2. As E(x) shifts further towards less negative values, $i_H(x)$ decreases while $i_{Fe}(x)$ increases gradually. At the limit of $i_H(x) = i_{Fe}(x)$ the value of E(x) equals the free corrosion potential of the system existing inside the crack, as shown in Figure 2. One can easily use Equations 5 and 7 to calculate $i_H(x)$ and $i_{Fe}(x)$, respectively, at various distances into the crack.

Figure 3 shows that under these conditions iron dissolution occurs at distances into the crack of $x \geq 0.04$ cm i.e., 400 μm. Thus, for cracks of L=10 or 100 μm depth under the present conditions (i.e., $a = 10^{-2}$ cm, E(0) = -0.5V (NHE), the entire depth of the crack will be cathodically protected

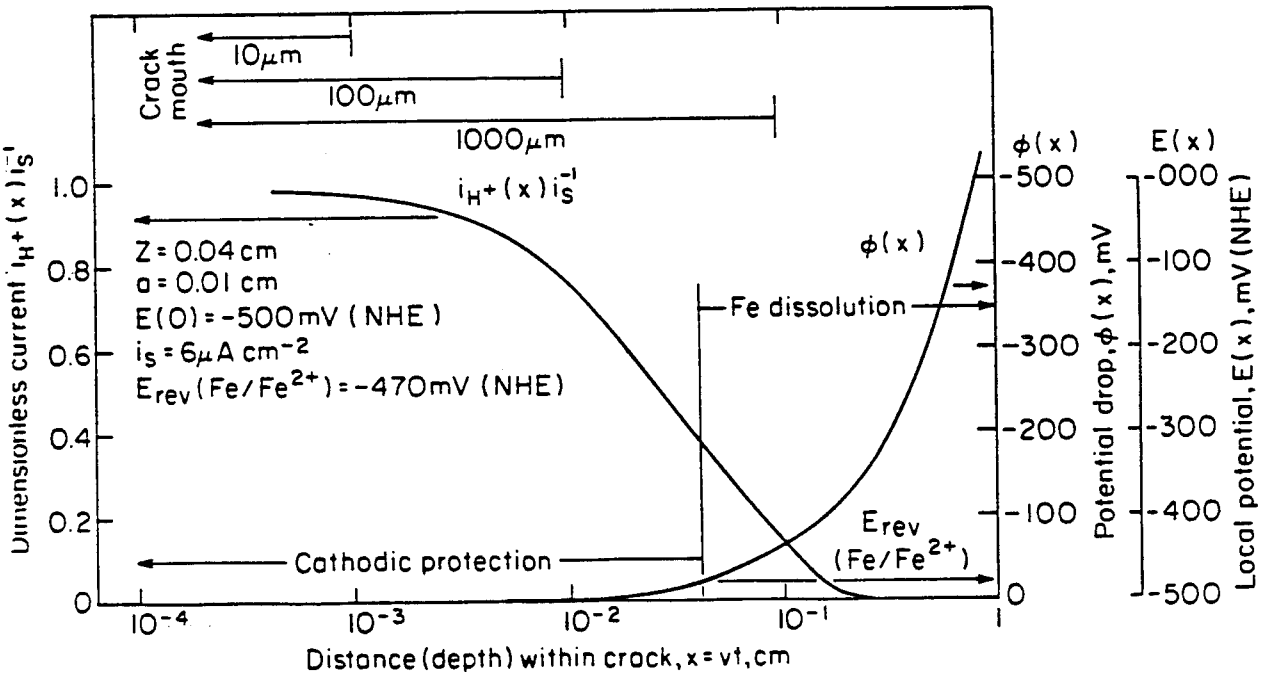

Figure 3. Potential and HER current distributions within cracks of various depths for a value of the characteristic depth Z = 0.04 cm during cathodic polarization of the iron surface (see text).

(see below for $a << 10^{-2}$cm or E(0) < -0.5V(NHE)). On the other hand, for a crack of 0.1 cm depth (1000 μm), only the top 60% of its flanks will be under cathodic protection. The bottom 40% will be undergoing simultaneous anodic dissolution and hydrogen evolution at rates which are dependent on distance, as discussed above. Alternatively, for a 1 cm deep crack, only the top 4% of its depth is under cathodic protection while the rest is undergoing anodic dissolution. Using the E(x) value calculated from Eq. 1 and a knowledge of the active/passive behavior as a function of pH, it can be determined if the anodic metal dissolution undergoes active or passive dissolution as a function of distance into the crack (or cracking time), as reported elsewhere for crevice corrosion (14).

Figures 4 and 5 illustrate the effects of one order of magnitude decrease in Z, i.e., for Z = 0.004 cm. This decrease in Z was brought about in two different ways, i.e., by decreasing a from 10^{-2} to 10^{-4} cm in Fig. 4, keeping E(0) = -0.500V (NHE) and all other parameters constant, Figure 4; and by changing E(0) from -0.50 to -0.72 (NHE) while keeping $a = 10^{-2}$ cm and the other parameters constant, Figure 5. For the case of $a = 10^{-4}$ cm in Fig. 4, the distance beyond which iron dissolution occurs becomes much shorter, being in this case only about 0.004 cm, i.e. 40 μm. Under this condition iron dissolution occurs at distances greater than 40 μm. Consequently, for any crack of a depth less than 40 μm (for the conditions of Fig. 4), the entire crack depth will be under cathodic protection. Similarly, for the conditions in Fig. 5, cracks will be fully protected if less than 400 μm in depth. Conversely, for a 1 cm deep crack, only the top 4% of its depth will be under cathodic protection while its interior (96% of its depth) will be involved in anodic dissolution.

For very narrow cracks (a=100 Å and E(0) = -0.5 (NHE)) only the top 1.6 μm of cracks of any depth will be under cathodic protection, the rest being involved in anodic dissolution.

Conclusions

The present analysis of the diffusion-migration problem within environmentally assisted cracks leads to the following conclusions:

1. The current and potential are nonuniformly distributed within cracks. A characteristic depth Z was derived which combines the important parameters of the system, and affects these distributions,

$$Z = \left[\frac{FD_{H^+} c^{o}_{H^+} a}{i_{oH}} \exp\frac{(\beta\eta(0))}{b}\right]^{1/2} \text{cm}$$

2. For conditions of cathodic polarization at the external metal surface, the potential within the crack shifts in the noble direction towards a limiting value, as a result of the potential shift (IR) mechanism. The nature of this limiting value of potential is different for active than for noble metals.

3. This potential shift leads to significant decreases in the rate of hydrogen evolution on the flanks of the crack.

4. For active metals, the potential shift may become sufficiently large to promote anodic dissolution within the crack even though the external metal surface is under cathodic protection.

5. The most general case involves nonuniform distributions of both the cathodic and anodic reactions on the flanks of cracks.

6. An initial crack in an active metal may remain under cathodic protection until its aspect ratio, $L\,a^{-1}$ or depth L (for a constant opening dimension a) reaches a certain critical value when the potential at L shifts to the region of metal dissolution. This critical depth depends on the value of a, the properties of the environment and on the polarization at the metal surface through the characteristic depth Z.

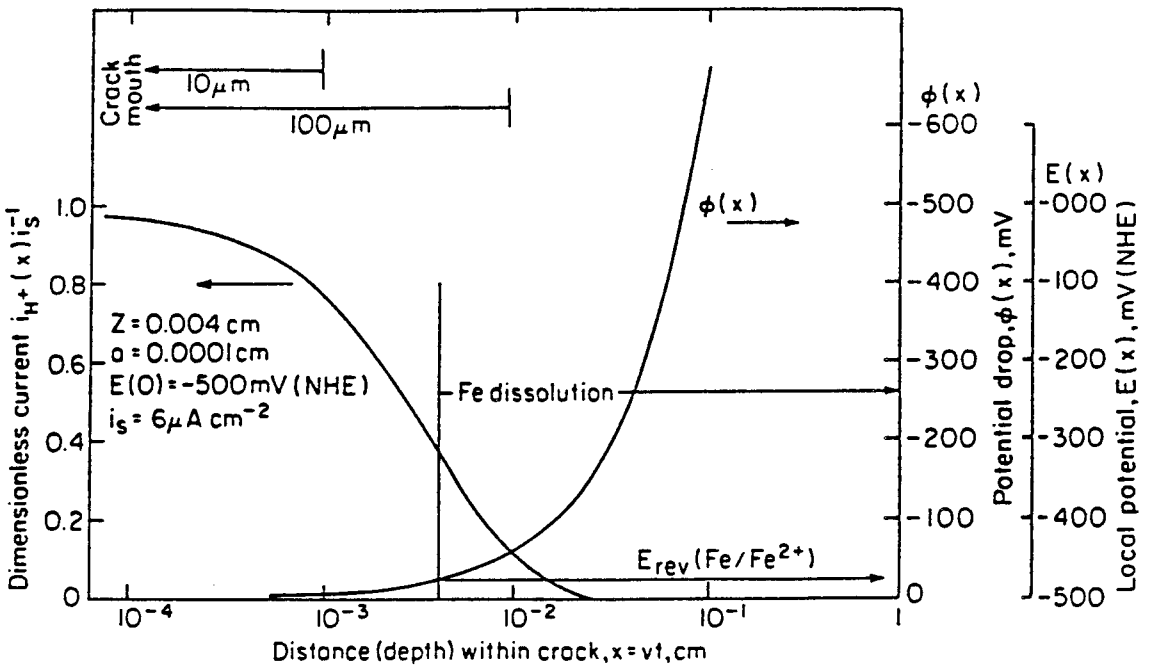

Figure 4. Effect of the decrease in crack opening dimesion *a* on the potential and current distributions for the conditions in Fig. 3.

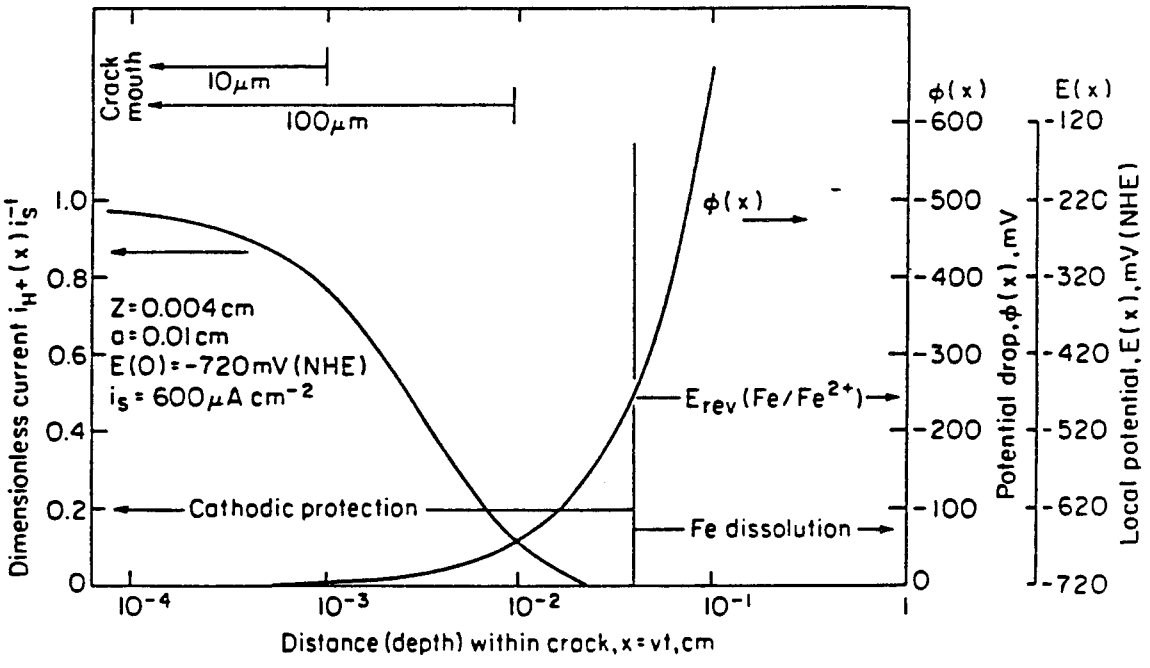

Figure 5. Effect of the decrease in cathodic polarization at the outer surface, E(0), on the potential and current distributions for the conditions in Fig. 3.

Acknowledgment

The authors acknowledge financial support of the Office of Naval Research, under Grant No: N00014-94-1-0086 (A. J. Sedriks) and of the National Science Foundation, Division of International Programs.

References

1. S. M. Bruemmer, et.al., ed., Parkins Symposium on Fundamental Aspects of Stress Corrosion Cracking (Warrendale, PA: TMS 1992).

2. Richard P. Gangloff and M. Brian Ives, ed., Environment - Induced Cracking of Metals, (Houston, TX: NACE, 1990).

3. R. W. Revie, "Environmental Cracking of Metals: Electrochemical Aspects, " Modern Aspects of Electrochemistry, B. E. Conway, J. O'M. Bockris and R. E. White, ed., 26 (1994) 277-337.

4. A. Turnbull, "The Solution Composition and Electrode Potential in Pits, Crevices and Cracks," Corros. Sci. 23 (1983), 833-870.

5. Z. Szklarska-Smialowska, Pitting Corrosion of Metals, (Houston, TX: NACE, 1986).

6. B. F. Brown, C. T. Fuji and E. P. Dahlberg, "Methods for Studying the Solution Chemistry Within Stress Corrosion Cracks," J. Electrochem. Soc. 116 (1969), 218-219.

7. D. D. Macdonald and M. Urquidi-Macdonald, "A Coupled Environment Model for Stress Corrosion Cracking in Sensitized Type 304 Stainless Steel in LWR Environments," Corros. Sci. 32 (1991), 51-81.

8. J. R. Galvele, "Transport Processes and the Mechanism of Pitting of Metals," J. Electrochem. Soc., 123 (1976), 464-474.

9. H. W. Pickering and R. P. Frankenthal, "On the Mechanism of Localized Corrosion of Iron and Stainless Steels," J. Electrochem. Soc., 119 (1972), 1297-1304.

10. B. G. Ateya and H. W. Pickering, "On the Nature of Electrochemical Reactions at a Crack Tip during Hydrogen Charging of a Metal," J. Electrochem. Soc., 122 (1975), 1018-1026.

11. C. Wagner and W. Traud, "Über Die Deutung von Korrosions-Vorgängen Durch Überlagerung von Elektrochemischen Teilvorgängen und Überdle Polentialbildung an Mischelektroden," Z. Elektrochem., 44 (1937), 391-402.

12. C. Wagner, "Calculation of the Current Distribution at Electrodes Involving Slots," Plating, 48 (1961), 997-1002.

13. B. G. Ateya and H. W. Pickering, "Electrochemical Processes Within Cavities and Their Relation to Pitting and Cracking," Hydrogen in Metals, vol 2, Ed., I. M. Bernstein and A. W. Thompson, (Metals Park, OH: ASM, 1974), 207-222.

14. Y. Xu and H. W. Pickering, "The Initial Potential and Current Distributions of the Crevice Corrosion Process," J. Electrochem. Soc., 140 (1993), 658-668; Y. Xu, M. Wang and H. W. Pickering, "On Electric Field Induced Breakdown of Passive Films and the Mechanism of Pitting Corrosion," ibid, 3448-3457.

Applied Surface Science 67 (1993) 266–274
North-Holland

applied
surface science

Atomic hydrogen chemisorption on Si(100)(2 × 1) studied by FI-STM

Xiang-Dong Wang [a], H. Lu [b], T. Hashizume [a], H.W. Pickering [c] and T. Sakurai [a]

[a] *Institute for Materials Research (IMR), Tohoku University, Sendai 980, Japan*
[b] *Laboratory for Surface Physics, Academia Sinica, Beijing 100080, People's Republic of China*
[c] *Department of Materials Science and Engineering, The Pennsylvania State University, University Park, PA 16802, USA*

Received 9 August 1992; accepted for publication 9 October 1992

A field ion-scanning tunneling microscopy study on hydrogen chemisorption on the Si(100)(2 × 1) surface is presented. At low coverages, hydrogen atoms reside singly on top of the dimerised Si atoms, and are imaged brightly. The hydrogen chemisorption induces buckling of dimers, indicating the strong bonding between Si and H atoms. With increasing coverage, both the (2 × 1) monohydride and (1 × 1) dihydride phases were formed. The former is imaged dark compared with the unreacted Si dimers, due to the reduction of the density of electronic states near the Fermi level. Surface etching was also observed. It was found that the corrosion of the surface is modest in the monohydride phase, while during the formation of the dihydride phase, the corrosion becomes significant. The behavior of hydrogen desorption from the dihydride and monohydride phases was investigated as a function of annealing temperature. Our STM results support the mechanism that the desorbing H_2 molecules are formed by combination of two hydrogen atoms forming the dihydride phase. Upon annealing at elevated temperatures, the Si overlayer stripes are formed by desorption of hydrogen from the etching products and the rearrangement of the Si atoms.

1. Introduction

The chemisorption of atomic hydrogen on various silicon surfaces has been studied for several decades [1–4] because of its importance in both fundamental research and technological applications. For instance, it is well known that hydrogen passivates silicon surfaces by saturating the silicon dangling bonds, other electronically active defects and stabilizing grain boundaries, etc. In addition to that, the adsorption of hydrogen on Si surfaces also provides a model example for investigation of the surface reconstructions and bonding properties. Though atomic hydrogen adsorption on the Si(100)(2 × 1) surface has been extensively studied by various kinds of methods, many controversies still exist. Previous studies have confirmed the existence of three reconstructions induced by hydrogen adsorption at different conditions, i.e. (2 × 1) [2,5] (the monohydride phase), (1 × 1) [2] (the dihydride phase), and the (3 × 1) [3] phase. By modest adsorption of atomic hydrogen at room temperature or saturate adsorption at elevated temperature (about 250°C), the (2 × 1) phase can be formed, which is characterized by binding one hydrogen atom to the dangling bond on each dimerized silicon atom without breaking the dimer bond. By saturating the surface with hydrogen at room temperature, Sakurai and Hagstrum [2] discovered the (1 × 1) reconstruction and introduced the idea of the dihydride phase, which formed by adsorbing two hydrogen atoms on each Si atom accompanied by the interruption of the dimer bond. Yet, the geometry of the hydrogen atoms in this phase has not been identified unambiguously. Recently, Chabal and Raghavachari [3] found a new (3 × 1) phase at saturation coverage while holding the substrate temperature at about 100°C. This reconstruction is formed by an alternating arrangement of monohydride and dihydride rows and appears even more stable than either the monohydride phase or the dihydride phase over a certain range of chemical potential [6]. The electronic structures of the (2 × 1) monohydride phase and (1 × 1) dihydride phase have been investigated by

Sakurai and Hagstrum [2] and Ciraci et al. [7] using UPS, and by Maruno et al. [8,9] using EELS, etc. It was found that the hydrogen induced electronic states are located at about −12 and −10 eV with respect to the vacuum level for the monohydride phase and dihydride phase, respectively [2]. From TPD (temperature programmed desorption) [10] experiment, Gupta et al. derived that desorption of H_2 from both the monohydride and dihydride phases exhibits second-order kinetics. However a previous investigation [11] and more recent LITD (laser induced thermal desorption) experiment [12] suggested a first-order desorption kinetics for desorption of H_2 from both phases.

The corrosion of the surface upon hydrogen adsorption has also been noticed and investigated mainly by desorption experiments. The products of the reaction have been identified to be mainly SiH_3 and small fractions of Si_2H_6, Si_3H_8 and Si_4H_{10}, etc. [13], but the detailed process and etching mechanism are still unclear. Moreover, earlier conclusions were based on the data averaged over the macroscopic area. The observation of the surface structure in real space had not been possible until the invention of the scanning tunneling microscope by Binnig and Rohrer [14]. The STM has proven to be of great potential to study the surface geometry as well as the surface electronic states with atomic resolution in real space. Hamers et al. [15] imaged the monohydride phase produced by dissociative adsorption of NH_3 on the Si(100)(2 × 1) surface. The imaged feature was attributed to the tunneling current through the localized Si–H bonding orbitals with a sample bias of −2 V. However, Johansson et al. [16] concluded, based on their polarization-dependent ARPES experiment, that the highest energy position of this band was 4.7 eV below the Fermi level and that no H-induced structures should be visible at all in the energy ranging from 0 to −2 eV, in contrary to Hamers et al. their STM study. Recently, Boland reported the observation of the newly discovered (3 × 1) phase [17] and discussed the role of pairing in the recombinative desorption of hydrogen [18]. However, the understanding of this system is far from complete and many controversies remain unresolved.

In this paper, we will present our FI-STM investigations on the hydrogen chemisorption on the Si(100)(2 × 1) clean surface. In the following sections, after a brief description of our experimental arrangement, we will present the behavior of adsorbed hydrogen atoms at the initial stage of adsorption, then we will show the surface structure of the monohydride phase and dihydride phase, and the corrosion of the surface caused by hydrogen adsorption. Finally we will show the surface change upon desorption at different temperatures. The mechanism behind the presented results will also be discussed.

2. Experiment

The details of our FI-STM system have been described elsewhere [19]. Here is a brief description. Our FI-STM is a combination of a high performance scanning tunneling microscope (STM) and a room temperature field ion microscope (FIM) which is used for the precise characterization of the scanning tip and its atomic scale fabrication. The entire STM setup is suspended with three 100 cm long springs and a 12-piece set of magnetic eddy current dampers which is attached beneath the STM set. The entire FI-STM chamber is mounted on the so-called active damper. By doing so, the troublesome resonance frequencies at 1–3 Hz are completely eliminated, making it possible to operate the STM stably and reliably. The use of the ⟨111⟩ oriented single crystal tungsten tip provides us with needed stability and long-lifetime of several months with daily operation. The main UHV chamber is pumped by a 1200 ℓ/s custom-design Riber ion pump and the base pressure is below 3×10^{-11} Torr except for the time of annealing the sample up to 1220°C. The pressure rise during the final annealing does not go beyond 1×10^{-10} Torr with this fast pumping system.

The Si(100) sample used was cut into a 4 × 19 mm^2 piece from a Sb doped n-type commercial Si(100) wafer with ρ about 0.07 $\Omega \cdot$ cm. Prior to introducing the sample into the UHV FI-STM chamber, only washing with methyl-alcohol was administered for sample cleaning. Cleaning the

sample in the UHV preparation chamber (which is attached to the main chamber) was carried out by a series of heating up to 1220°C following the 5 hour's degassing at 700°C. In this way, the clean Si(100)(2 × 1) surface with a minimum density of defects was obtained. The temperature was measured by an infrared pyrometer.

The atomic hydrogen dosing was achieved by introducing high purity H_2 gas into the UHV chamber through an adjustable leak valve, passing through the hot tungsten ribbon which was heated up to 1500°C to dissociate molecular hydrogen into atomic hydrogen. The H_2 dosage, which was given in Langmuir units, was used only as a measure for the atomic hydrogen deposition rate. It was ensured that the hot tungsten ribbon did not damage the vacuum during H exposure. The hydrogen adsorption was performed by holding the sample at room temperature. Some temperature rise in the sample surface was expected during the H adsorption, however, the temperature rise was not high enough to cause desorption of atomic hydrogen from the surface. The STM images were taken at least 3 h after the annealing to avoid the effect of thermal drift. A sample bias between −3 and +3 V was used, the tunneling current was kept constant at 20 pA and the scanning rate was 450 Å/s during the normal STM operation.

3. Results and discussion

3.1. Properties of the initial stage of hydrogen adsorption

Fig. 1 is a typical STM topography of atomic hydrogen adsorbed on the Si(100)(2 × 1) surface at a very low coverage (~ 0.03 ML). The surface is characterized by the bright round spots sitting on top of the buckled dimers and distributed randomly on the surface. At both sides of these bright spots, the dimers are also buckled, imaged brighter than the unbuckled dimer chains. Based on the fact that the number density of these bright spots increases with the hydrogen dosage, these are concluded to be the image of hydrogen atoms. This is basically consistent with the result

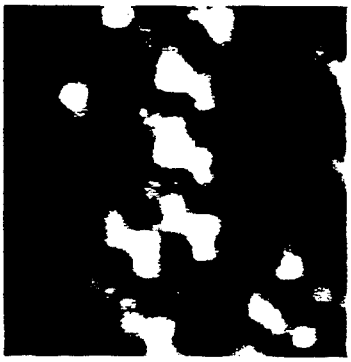

Fig. 1. STM topography of Si(100)(2 × 1) surface covered by about 0.03 ML of atomic H, sample bias V_s = 1.6 V.

reported by Boland [18], though he could not observe the buckling of the dimers adjacent to the hydrogen atoms. A question is, is it hydrogen atoms that prefer to stay on buckled dimers or is the buckling of the dimers induced by the adsorbed hydrogen atoms? From the following argument, we conclude that it is hydrogen atoms that induce the buckling of the dimers adjacent to them, though it is still possible that H atoms prefer to stay on buckled dimers. First, by comparing the density of the buckled dimers before and after adsorption, it was found that the density of this kind of buckled dimers increased with increasing H dosage. Second, adatom-like protrusions without buckling of the adjacent dimers were rarely found. The buckling of the dimers on the Si(100)(2 × 1) surface has been of interest for many years and there are controversies between the results obtained from STM and other techniques. Results from the STM [20] have suggested that the surface seems mostly unbuckled. However, it has been revealed that the energy difference between the buckled dimer and the unbuckled dimer is small enough so that the STM imaged symmetric dimers may in fact be the time average of rapidly oscillating asymmetric (buckled) dimers with charges transferring back and forth between two dimerized atoms [21,22], while dimers can be stably buckled in the vicinity of steps and various kinds of point defects [20]. The fact that the H atoms are almost adsorbed singly instead of in pairs at low coverage indicates the significant strong bonding between the H atom

and the dangling bond of one of the dimerized Si atoms. This also indicates that most of the arrived H adatoms adsorbed on the dangling bonds without moving around. So the periodicity and the symmetry around the adsorption site no longer exist due to this strong bonding as well as the saturation of the dangling bond by adsorbed hydrogen atom. This causes a charge redistribution, which is likely to induce the buckling of the dimers nearby. Similar results were also obtained for alkali-metal adsorption on the Si(100)(2 × 1) surface [23] by STM. From the number of buckling dimers induced by H adsorption, we suggest that the interaction between the H atom and the Si substrate is of short range, i.e., limited to one or two dimers near the adsorbed H atom. It is interesting and important to study the interaction between the singly adsorbed hydrogen atoms with surface silicon atoms as well as the interactions among the adsorbed hydrogen atoms through the investigation of the initial stage of hydrogen adsorption, which may reveal the mechanism of the desorption process [18]. However, up to now, little work has been done on it, which limits our further discussion. We hope our results will stimulate further investigations of the detailed properties of the Si–H bond, such as the charge transfer, bond length, electronic states, etc.

3.2. Formation of the monohydride phase and dihydride phase

Figs. 2a–2d are the STM images showing the changes of the surface structure with increasing H_2 coverage. Fig. 2a is the image obtained after 24 L adsorption, the coverage is estimated to be approximately 0.3 ML. In this case, the surface is characterized by the interruption of the dimer chain by dark areas and the buckling of almost all the dimers on the surface which imaged bright.

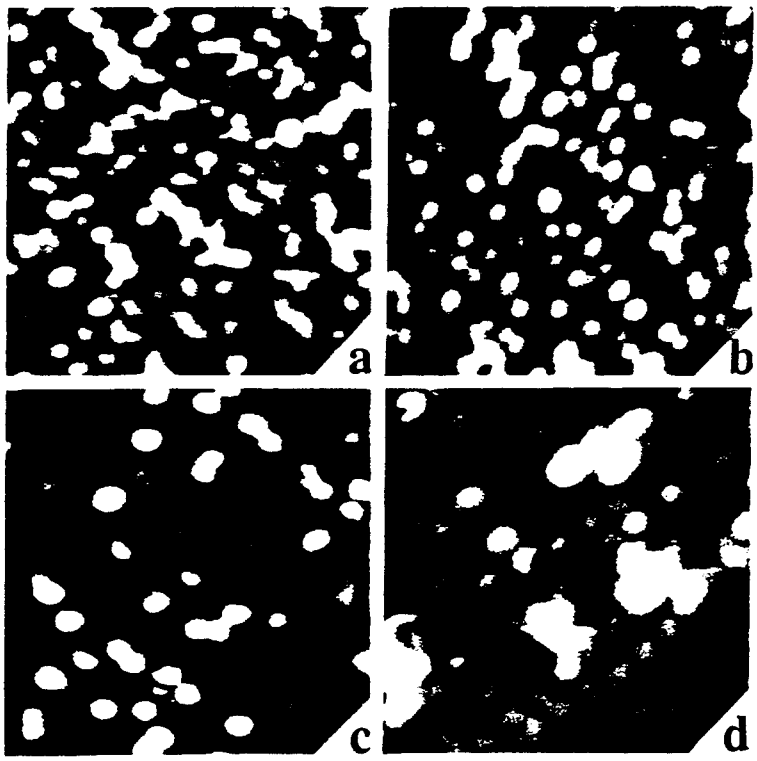

Fig. 2. Si(100) surface structures after hydrogen adsorption at different dosages. (a) After adsorption of 24 L, $V_s = -2.0$ V, (b) after adsorption of 48 L, $V_s = -3.0$ V, (c) after adsorption of 108 L, $V_s = -1.6$ and (d) after adsorption of 2000 L, $V_s = -2.0$ V. The area is about 100 × 100 Å^2 for (a)–(c) and about 43 × 43 Å^2 for (d), respectively.

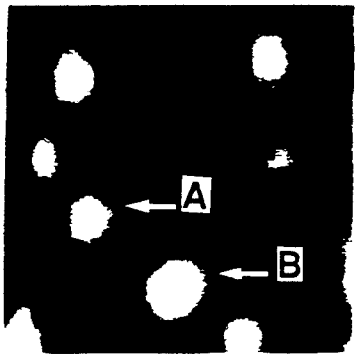

Fig. 3. The illustration of two different kinds of features, marked with "A" and "B", respectively. The image was obtained upon 48 L exposure. $V_s = -2.0$ V.

With increasing coverage, the area of dark contrast increases, as shown in fig. 2b, which was obtained upon 48 L exposure. In this case, the dimer chains in the dark area are well resolved, showing clearly that the dimers in the monohydride phase are imaged dark. This can be explained by the reduction of the electronic density of states near the Fermi level [25,26]. From the UPS results [7,24] and theoretical calculation [27], it is known that on the clean dimerized Si(100)-(2 × 1) surface, there exists a localized surface state near the Fermi level due to the dangling bond of the surface silicon atoms. This surface state is removed upon hydrogen adsorption by saturation of the dangling bonds, resulting in the reduction of the tunneling current.

When the surface is largely covered by the monohydride phase, the prominent feature is the bright dots on the well ordered (2 × 1) monohydride surface (see also fig. 2b). These bright dots can be grouped into two types, namely type A and B. Fig. 3 is a close-up illustrating typical images of dots "A" and "B", where "A" dots are located on the side of the dimer chains, while "B" dots are located on the dimer chains and imaged larger than "A" dots. According to the observation that (a) the dimers adjacent to "A" dots are rarely buckled, which is in contrast to the results in the initial stage of hydrogen adsorption, and that (b) the density of "A" dots decreased with the increase of the hydrogen coverage, we suggest that "A" dots represent the unpaired hydrogen atoms. Thus the unbuckling of the dimers adjacent to the "A" dots indicate the considerable passivation of the surface reactivity. On the other hand, the density of type "B" dots remains almost unchanged. Further increasing the dosage results in the formation of small amounts of clusters imaged slightly larger than "B" dots. Though the identification of the products by STM alone is not possible, we suggest that these type "B" dots are the products of reacted Si atoms with hydrogen, according to the thermal desorption results by Gates et al. [13], mainly SiH_3 with small amount of other species, such as Si_2H_6, Si_3H_8 and Si_4H_{10}. Fig. 2c, was obtained upon 108 L of hydrogen exposure, where type "A" dots were almost eliminated, while type "B" dots remained. It is also found from our STM investigation that these products spread randomly and almost separately on the surface, with little tendency to combine into larger clusters, indicating the absence of etching centers or nucleation centers of the reacted Si atoms. During the formation of the monohydride phase, the degree of surface etching is still limited within a low level, which let the monohydride phase form with higher order. Also in the case as shown in fig. 2c, it was found that the formation of a new phase, the dihydride phase, started, indicated by the splitting of the monohydride dimers.

With increasing dosage, the surface gradually shifts from the (2 × 1) monohydride phase to the dihydride phase. Fig. 2d shows the surface upon 2000 L of hydrogen adsorption. The surface is of the (1 × 1) reconstruction with a fraction of the (2 × 1) phase. We noticed that with the increase of the proportion of the (1 × 1) phase, the etching of the surface becomes more and more extensive, shown by the high density of missing atom defects and "B" dots. The difference between the sizes of the dots is slight, indicating that the bonding to the substrate is still strong enough to resist the migration of the reacted species.

3.3. Desorption of hydrogen

The understanding of the desorption properties of hydrogen is almost of the same importance as the adsorption process, especially in control-

ling of the epitaxial growth of the Si film on the Si(100) surface by CVD, as well as analyzing the surface etching process. For many years, several groups have studied the properties of the desorption process [10,12,13]. The desorption temperatures for hydrogen in the SiH species (β_1-state) and SiH_2 species (β_2-state) have been determined by several reports with similar conclusions. Gupta et al. [10] reported that for hydrogen adsorbed on porous silicon, which is similar to that on the Si(100) surface according to the similarities between the infrared spectra of hydrogen in both cases, the desorption of hydrogen in the β_1-state occurs at temperatures between 720 and 800 K (447 and 527°C), while the desorption of hydrogen in the β_2-state occurs at 640–700 K (367–427°C). From TPD spectra, Gates et al. [13] found that the peak temperature for H_2 desorption from the β_1-state is 540°C and the desorption starts at about 450°C, while the peak temperature for desorption of the β_2-state is 425°C and the desorption starts at about 370°C. So these results suggest the desorption of hydrogen starts about 370°C for the β_2-state and 450°C for the β_1-state. Gates et al. [13] also found that the desorption of the SiH_3 species occurs at about 375°C in the form of SiH_4, which is 50°C below the desorption peak of the β_2-state. The desorption of SiH_4 also results in the removal of the silicon atoms from the top of the surface. The TPD yield of SiH_4 saturates at the maximum value when the coverage increased beyond 0.5 ML. Recently, Boland [18] reported STM data on the behavior of the monohydride phase upon H desorption. However, controversies about the desorption kinetics and transition process from the dihydride phase to the monohydride phase remain. Information on the real space observation of the surface structure change upon H_2 desorption is still not sufficient, especially in the process of the desorption from the dihydride phase.

To investigate the desorption process of hydrogen from both the SiH_2 state (β_2) and SiH state (β_1), the surface was exposed to 1000 L of hydrogen prior to annealing at modest temperatures. As shown in fig. 4a, the surface is of mixture of the (1 × 1) and (2 × 1) phases. According to the temperature dependence of the H_2 desorption in each species, we performed sequential annealings, i.e. heating the sample for 1 min at temperatures: 320°C, 400°C, 460°C and 500°C.

Annealing the sample at 320°C resulted in no obvious changes in the surface structure, which is consistent with the TPD result at the same temperature, that is, almost all the adsorbed hydrogen atoms and reacted species remain on the surface. Though some of the hydrogen atoms may obtain sufficient energy to desorb from the surface due to the Boltzmann distribution of thermal energy, the amount is small in such a short time duration as was shown by an isothermal desorption experiment [10]. After further annealing of the sample at 400°C for 1 min, as shown in fig.

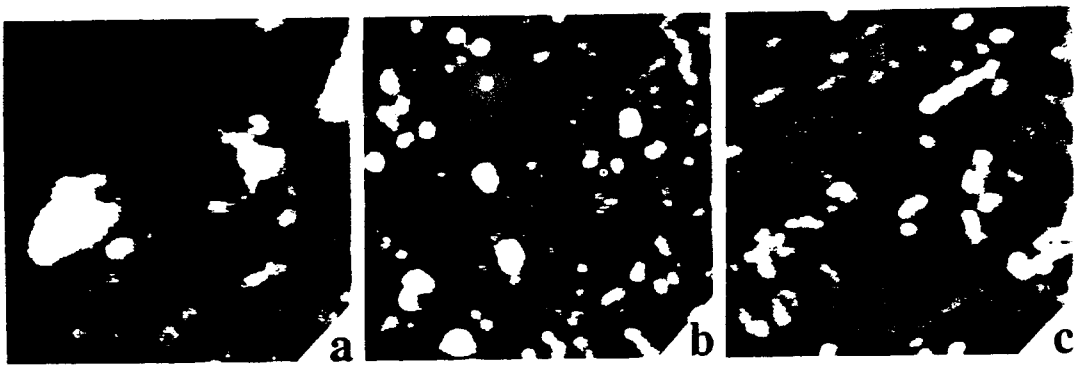

Fig. 4. Changes in surface structure upon annealing at different temperature. (a) Mixture of monohydrogen and dihydrogen after adsorption of 1000 L hydrogen without annealing, (b) after annealing at 400°C and (c) after annealing at 460°C. $V_s = -1.6$ V for all three. The area is about 150 × 150 Å^2 for (a) and (b), and about 43 × 43 Å^2 for (c), respectively.

4b, the surface is characterized by a high density of dark defects and some bright dots which made the surface look highly disordered. However, the direction of the dimer chain can still been identified, indicating that it is of the (2 × 1) reconstruction. We attribute this change to desorption of the hydrogen in the β_2-state, while the monohydride phase still exists. There exists controversy about the way of H_2 desorption from the dihydride state. Schulze et al. [11] and Masson et al. [28] had suggested that the desorbing H_2 was formed by the association of the two hydrogen atoms in the same SiH_2 species in order to explain the suggested first-order desorption kinetics. In contrast, theoretical work [29] assumed the desorption of H_2 from the dihydride species on Si(100) in terms of the recombinationary desorption of two hydrogen atoms from two adjacent silicon hydride species. In this case, the transition into the monohydride phase takes place spontaneously with the combination of hydrogen molecules. This model supported the second-order desorption kinetics obtained from the isothermal desorption experiment [10]. However, as can be seen in fig. 4b, the surface is highly disordered due to the interruption of the dimer chain by dark areas which are attributed to the monohydride phase from our previous analysis. This suggests that H_2 molecules desorb directly from the dihydride phase without shifting to the monohydride phase. Because of the complicated processes involved in the adsorption and desorption of hydrogen, though it might be difficult to rule out unambiguously one of the desorption models suggested above, we suggest, from the STM observation, that at least a large amount of hydrogen in the dihydride phase desorbs directly from the surface without transiting into the monohydride phase. Thus our STM result supports the assumption that the desorbing H_2 molecules are formed by the two hydrogen atoms in the same SiH_2 species instead of two adjacent SiH_2 species. This is in contradiction with TPD data [10,30], however, TPD data did not give an unambiguous answer to the kinetics of H_2 desorption in the dihydride phase as no TPD work gave the absolute coverage change before and after desorption of the dihydride phase. In fact, the desorption kinetics of H_2 from the Si(100) surface has not been well understood yet, the previous analysis of TPD data was merely based on the assumption that the dihydride phase transferred to monohydride phase by desorbing H_2 from two dihydride species. As to our knowledge, only Oura et al.

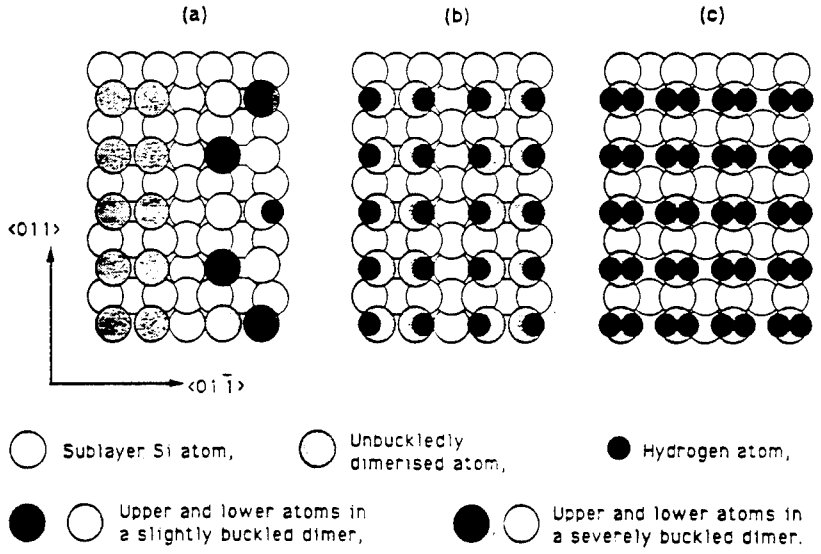

Fig. 5. Schematic of the adsorption geometry of hydrogen atoms, (a) initial stage of adsorption (proposed in this work). (b) (2 × 1) monohydride phase (ref. [2]), and (c) (1 × 1) dihydride phase (ref. [2]).

their work [31] shows the absolute coverage change of the adsorbate from 1.85 ML of hydrogen saturated (1 × 1) phase to 1 ML of the (2 × 1) monohydride phase. However, this result dose not have enough accuracy to convince people since an ideally saturated (1 × 1) phase should be 2 ML instead of 1.85 ML. Furthermore, no other work has ever been published to support this conclusion.

Upon further annealing of the sample at 460°C for 1 min, the surface is as shown in fig. 4c, which is dominated by the (2 × 1) structure with ordered dimer chains, although the density of defects is still higher than that on the clean surface. A novel feature in fig. 4c is the formation of the adatom lines on the substrate terraces, while the number of bright dots decreases considerably, indicating the re-formation of the clean Si(100)(2 × 1) surface. By correlating the disappearance of the bright dots and the formation of the adatom lines, we attribute these adatom lines to Si atoms that formed by desorption of hydrogen from SiH_3 and small amounts of other species. The mobility of dissociated Si atoms is high enough so that the Si atoms can combine with each other with high probability, forming epitaxial dimer lines perpendicular to the direction of the dimer lines of the substrate. Further annealing of the sample at 500°C results in no obvious changes in the surface structure, indicating that the critical temperature for Si overlayer formation is between 400°C and 460°C.

4. Summary

Our STM investigations of H adsorption on the Si(100)(2 × 1) surface can be summarized as follows (see fig. 5 for illustration).

(1) At low coverages (below 10% of a monolayer), single hydrogen atoms reside on the top of the dimerized surface Si atoms, imaged as bright spots. Those H atoms also induce the buckling of the dimers at both sides of the adsorbed hydrogen atom.

(2) With increasing coverage, the density of hydrogen atoms which adsorb in pairs increases. The monohydride phase is imaged dark compared with unreacted Si dimers because of the reduction of the density of states near the Fermi level.

(3) Our data suggest that the reacted Si atoms, mainly SiH_3, are imaged as bright dots, spreading randomly on the dimer chain. At the monohydride phase, the surface etching is slight, while upon the formation of the dihydride phase, the corrosion of the surface becomes significant. It seems that the etching originates and expands randomly without any preferred sites.

(4) Upon annealing a surface having a mixture of the (1 × 1) and (2 × 1) phases at different temperatures, the changes in the surface structure were observed. Upon annealing at 400°C, the dihydride phase disappeared while the monohydride phase still existed. Our results support the assumption that the desorbing H_2 molecules are formed by combination of two hydrogen atoms in the same SiH_2 species. Upon annealing the sample above 460°C, the (2 × 1) monohydride phase disappeared, the surface is dominated by the Si(2 × 1) dimers with overlayer stripes formed by the recombination of Si atoms through the dissociation of SiH_3 species. **Sponsor [32].**

References

[1] J.T. Law, J. Chem. Phys. 30 (1959) 1568.
[2] T. Sakurai and H.D. Hagstrum, Phys. Rev. B 14 (1976) 1593.
[3] Y.J. Chabal and K. Raghavachari, Phys. Rev. Lett. 54 (1985) 1055.
[4] J.A. Schaefer, Surf. Sci. 178 (1986) 90.
[5] H. Ibach and J.E. Rowe, Surf. Sci. 43 (1974) 481.
[6] J.E. Northrup, Phys. Rev. B 44 (1991) 1419.
[7] S. Ciraci, R. Butz, E.M. Oellig and H. Wagner, Phys. Rev. B 30 (1984) 711.
[8] S. Maruno, H. Iwasaki, K. Horioka, S.-T. Li and S. Nakamura, Surf. Sci. 123 (1982) 18.
[9] S. Maruno, H. Iwasaki, K. Horioka, S.-T. Li and S. Nakamura, Phys. Rev. B 27 (1983) 4110.
[10] P. Gupta, V.L. Colvin and S.M. George, Phys. Rev. B 37 (1988) 8234.
[11] G. Schulze and M. Henzler, Surf. Sci. Lett. 124 (1983) 336.
[12] K. Sinniah, M.G. Sherman, L.B. Lewis, W.H. Weinberg, J.T. Yates, Jr. and K.C. Janda, J. Chem. Phys. 92 (1990) 5700; Phys. Rev. Lett. 62 (1989) 567.
[13] S.M. Gates, R.R. Kunz and C.M. Greenlief, Surf. Sci. 207 (1989) 364.

[14] G. Binnig and H. Rohrer, Helv. Phys. Acta 55 (1982) 726.
[15] R.J. Hamers, Ph. Avouris and F. Bozso, Phys. Rev. Lett. 59 (1987) 2071.
[16] L.S.O. Johansson, R.I.G. Uhrberg and G.V. Hansson, Phys. Rev. B 38 (1988) 13490.
[17] J.J. Boland, Phys. Rev. Lett. 65 (1990) 3325.
[18] J.J. Boland, Phys. Rev. Lett. 67 (1991) 1539.
[19] T. Sakurai, T. Hashizume, Y. Hasegawa, I. Kamiya, N. Sano, K. Yokoyama, H. Tanaka, I. Sumida and S. Hyodo, J. Vac. Sci. Technol. A 8 (1990) 324;
T. Sakurai, T. Hashizume, I. Kamiya, Y. Hasegawa, N. Sano, H.W. Pickering and A. Sakai, Prog. Surf. Sci. 33 (1990) 3.
[20] R.J. Hamers, R.M. Tromp and J.E. Demuth, Phys. Rev. B 34 (1986) 5343.
[21] G.P. Kochanski and J.E. Griffith, Surf. Sci. Lett. 249 (1991) L293.
[22] P.C. Weakliem, G.W. Smith and E.A. Carter, Surf. Sci. Lett. 232 (1990) L219.
[23] T. Hashizume, Y. Hasegawa, I. Sumita and T. Sakurai, Surf. Sci. 246 (1991) 189.
[24] F.J. Himpsel and D.E. Eastman, J. Vac. Sci. Technol. 16 (1979) 1297.
[25] J. Tersoff and D.R. Hamann, Phys. Rev. Lett. 50 (1983) 1998.
[26] J. Tersoff, Phys. Rev. B 39 (1989) 1052.
[27] H.H. Madden, Surf. Sci. 105 (1981) 129.
[28] D. Masson, L. Paquin, S. Poulin-Dandurand, E. Sacher and A. Yelon, J. Non-Cryst. Solids 66 (1984) 93.
[29] S. Ciraci and I.P. Batra, Surf. Sci. 178 (1986) 80.
[30] C.C. Cheng and J.T. Yates, Jr., Phys. Rev. B 43 (1991) 4041.
[31] K. Oura, J. Yamane, K. Umezawa, M. Naitoh, F. Shoji and T. Hanawa, Phys. Rev. B 41 (1990) 1200.

[32] Sponsored in part by Office of Naval Research, Contract No. N00014-91-J-1189.

June 1993

BASIC DISTRIBUTION LIST

Technical Reports and Publications

Organization	Copies
Defense Technical Information Center Cameron Station Alexandria, VA 22304-6145	2
Office of Naval Research 800 N. Quincy Street Arlington, VA 22217-5660 ATTN: Code 3310	3
Naval Research Laboratory 4555 Overlook Ave, S.W. Washington, DC 20375 ATTN: Code 6000	1
Code 6300	1
Code 5227	1
Naval Air Warfare Center White Oak Detachment Silver Spring, MD 20903-5000 ATTN: Library	1
Code R33	1
Naval Postgraduate School Monterey, CA 93940 ATTN: Mechanical Engineering Department	1
Naval Air Systems Command Washington, DC 20361 ATTN: Code 5304	1
Naval Sea Systems Command Washington, DC 20362 ATTN: Code 05M	1
Code 05R	1

Organization	Copies
Naval Air Warfare Center Aircraft Division, Trenton Trenton, NJ 08628 ATTN: Library	1
Naval Facilities Engineering Service Center Port Hueneme, CA 94043 ATTN: Materials Div.	1
Naval Surface Warfare Center Carderock Division Bethesda, MD 20084 ATTN: Library	1
Naval Underwater Warfare Ctr. Newport, RI 02840 ATTN: Library	1
Naval Air Warfare Center Weapons Division China Lake, CA 93555-6001 ATTN: Library	1
NASA Lewis Research Center 21000 Brookpark Road Cleveland, OH 44135 ATTN: Library	1
National Institute of Standards and Technology Gaithersburg, MD 20899 ATTN: Metallurgy Division	1
Ceramics Division	1
Fracture & Deformation Division	1

Organization	Copies
Naval Command, Control and Ocean Surveilance Center R&D Division San Diego, CA 92152-5000 ATTN: Library	1
Office of the Assistant Commander HQ Marine Corps 2 Navy Annex Washington, DC 20380-1775 ATTN: Scientific Advisor	1
Army Research Office P.O. Box 12211 Research Triangle Park, NC 27709 ATTN: Metallurgy & Ceramics Program	1
Army Materials Technology Laboratory Watertown, MA 02172-0001 ATTN: SLCMT-TMM	1
Air Force Office of Scientific Research Building 410 Bolling Air Force Base Washington, DC 20332 ATTN: Electronics & Materials Science Directorate	1
NASA Headquarters Washington, DC 20546 ATTN: Code RN	1
Naval Surface Warfare Center Port Hueneme Division 4363 Missile Way Port Hueneme CA 93043-4307 ATTN: Library	1
Metals Information Analysis Center Purdue University 2595 Yeager Road West Lafayette IN 47906	1

Organization	Copies
Naval Facilities Engineering Command Alexandria, VA 22331 ATTN: Code 03	1
Oak Ridge National Laboratory Metals and Ceramics Div. P.O. Box X Oak Ridge, TN 37380	1
Los Alamos Scientific Lab. P.O. Box 1663 Los Alamos, NM 87544 ATTN: Report Librarian	1
Argonne National Laboratory Metallurgy Division P.O. Box 229 Lemont, IL 60439	1
Brookhaven National Laboratory Upton, Long Island NY 11973 ATTN: Research Library	1
Lawrence Berkeley Lab. 1 Cyclotron Rd Berkeley, CA 94720 ATTN: Library	1
Naval Surface Warfare Center Annapolis Detachment Annapolis, MD 21402-5067 ATTN: Code 61 Code 613 Code 0115	1 1 1

4315DIST
04 June 1993

Supplemental Distribution List

Profs. G.H. Meier and F.S.Pettit
Dept. of Mat'ls Science & Eng.
848 Benedum Hall
University of Pittsburgh
Pittsburgh, PA 15261

Dr. G. D. Davis
Martin Marietta Laboratories 848
1450 South Rolling Rd.
Baltimore, MD 21227-3898

Prof. Gordon P. Bierwagen
North Dakota State University
Dept. of Polymers and Coatings
Box 5227
Fargo, ND 58105

Dr. S.M. Lipka
Dept. of Ocean Engineering
Florida Atlantic University
Boca Raton, FL 33431-0991

Prof. H.W. Pickering
The Pennsylvania State Univ.
209 Steidle Bldg.
University Park, PA 16802

Dr. D.D. Macdonald
The Pennsylvania State Univ.
517 Deike Bldg.
University Park, PA 16802

Prof. D.J. Duquette
Dept. of Metallurgical Eng.
Rensselaer Polytechnic Inst.
Troy, NY 12181

Dr. B.G. Pound
SRI International
333 Ravenswood Ave.
Menlo Park, CA 94025

Prof. D. Tomanek
Michigan State University
Dept. of Physics and Astronomy
East Lansing, MI 48824-1116

Prof. C.R. Clayton
Dept. of Materials Science & Eng.
State University of New York
Stony Brook
Long Island, NY 11794

Dr. M. W. Kendig
Rockwell International Sci.Ctr.
1049 Camino Dos Rios
P.O. Box 1085
Thousand Oaks, CA 91360

Dr. J.W. Oldfield
Cortest Laboratories Ltd
23 Shepherd Street
Sheffield, S3 7BA, U.K.

Prof. R. A. Rapp
Dept. of Metallurgical Eng.
The Ohio State University
116 West 19th Avenue
Columbus, OH 43210-1179

Ms. D.M. Aylor
Code 613
Naval Surface Warfare Center
Annapolis, MD 21402-5067

Dr. R.D. Granata
Sinclair Laboratory #7
Lehigh University
Bethleham, PA 18015

Prof. K. Sieradzki
Dept. of Materials Sci. & Eng.
The Johns Hopkins University
Baltimore, MD 21218

Dr. P.S. Pac
Code 6326
Naval Research Laboratory
Washington, D.C. 20375-5343

Dr. W.P. Allen
United Technologies Research Ctr.
East Hartford, CT 06108

Dr. B.A. Shaw
Dept. of Eng. Sci. & Mechanics
207 Hallowell Building
The Pennsylvania State University
University Park, PA 16802-1484

Dr. P. Cox
SRI International
333 Ravenswood Ave.
Menlo Park, CA 94025-3493

Dr. R. E. Ricker
National Institute of Standards and Technology
Bldg. 223, Room B-266
Gaithersburg, MD 20899

Dr. F.B. Mansfeld
Dept. of Materials Science
University of Southern California
University Park
Los Angeles, CA 90089-0241

Prof. R.E. White
Dept. of Chemical Engineering
University of South Carolina
Columbia, SC 29208

Prof. R.A. Buchanan
Dept. of Materials Science & Eng.
University of Tennessee
Knoxville, TN 37996-2200

Dr. B.J. Little
NRL Detachment
Bldg. 1105, Room D415
Stennis Space Center
MS 39529-5004

Prof. M.E. Orazem
Dept. of Chemical Engineering
University of Florida
Gainesville, FL 32611

Prof. J. O'M. Bockris
Dept. of Chemistry
Texas A & M University
College Station, TX 77843

Dr. V. S. Agarwala
Code 6062
Naval Air Warfare Center
Warminster, PA 18974-0591

Prof. R.C. Newman
UMIST
Corrosion and Protection Center
P.O. Box 88
Manchester M60 1QD, U.K.

Prof. S. C. Dexter
College of Marine Studies
University of Delaware
700 Pilottown Rd
Lewes, DE 19958

Prof. R.P. Gangloff
Dept. of Mat'ls Science & Eng.
Thornton Hall
University of Virginia
Charlottesville, VA 22903-2442

Dr. R. Brown
Dept. of Chemical Engineering
University of Rhode Island
Kingston, R.I. 02881-0805

Dr. J. Jones-Meehan
Code R301
Naval Surface Warfare Center
10901 New Hampshire Ave.
Silver Spring, MD 20903

Dr. P. Natishan
Code 6322
Naval Research Laboratory
Washington, D.C. 20375-5343

Dr. R. L. Jones
Code 6170
Naval Research Lab.
Washington, D.C. 20375-5342